

# 1      Hydrothermal Plume Near-Field Dynamics from LES 2      and Observations

3      Cyprien Lemaréchal<sup>1</sup>, Guillaume Roullet<sup>1</sup>, Jonathan Gula<sup>1,2</sup>

4      <sup>1</sup>Univ Brest, CNRS, Ifremer, IRD, Laboratoire d'Océanographie Physique et Spatiale (LOPS), IUEM,  
5      F29280, Plouzané, France  
6      <sup>2</sup>Institut Universitaire de France (IUF), Paris, France

## 7      Key Points:

- 8      • Hydrothermal plumes exhibit strong mixing reflected by significant vertical and  
9      temporal variability in entrainment rate in the near-field
- 10     • Plume theory cannot be applied directly since forced and lazy plumes are in a transi-  
11     tional state at the scale of hydrothermal edifices
- 12     • Short exposure times to high temperatures suggest that biological materials can  
13     be transported through the plume without lethal effects

---

Corresponding author: Guillaume Roullet, [rouplet@univ-brest.fr](mailto:rouplet@univ-brest.fr)

14 **Abstract**

15 Hydrothermal plumes play a crucial role in vent fields by injecting significant buoyancy  
 16 flux from centimeter-scale vents and rising hundreds of meters, yet their near-field dy-  
 17 namics remain poorly understood. Using a Large-Eddy Simulation approach with adap-  
 18 tive mesh refinement, we study these plumes at centimeter-scale resolution within a 6  
 19 m domain above the vent. We first study a typical black smoker in the forced plume regime  
 20 to quantify the mean flow and spatial variability, investigating the link between turbu-  
 21 lent structures and the entrainment rate  $\alpha$  of surrounding water. Significant vertical and  
 22 temporal variability in  $\alpha$  is observed, with an overall value of  $\alpha = 0.19$ . The results are  
 23 compared with in-situ data and plume theory. Next, we investigate the sensitivity of the  
 24 flow field to source parameters, characterizing the transition between forced or lazy plume  
 25 regimes and the pure plume regime. In the far-field, plumes achieve self-similarity and  
 26 the flow field is consistent with theoretical plume scalings, showing a dependence on source  
 27 buoyancy flux for predictions in this region. The extent of the transition region where  
 28 plume self-similarity breaks down is defined, and its importance in the context of in-situ  
 29 observations is highlighted. Finally, we show that extreme temperatures above 100°C oc-  
 30 cur in the first two meters of the column, but exposure times for a proxy tracer are short,  
 31 suggesting that hydrothermal plumes could serve as viable transport vectors for biolog-  
 32 ical materials.

33 **Plain Language Summary**

34 Hydrothermal vent fields on the ocean floor release hot, mineral-rich water that forms  
 35 rising plumes, known as black smokers. These plumes are critical to the unique ecosys-  
 36 tems around vents (the source points) and influence how heat and materials spread through  
 37 the ocean. However, the details of plume behavior near the seafloor, where they are most  
 38 energetic, remain poorly understood. Using advanced computer simulations, we stud-  
 39 ied these plumes at high resolution, focusing on the region close to the vent. We exam-  
 40 ined how the plumes mix with the surrounding water and found that the mixing rate changes  
 41 significantly with height and time. The results were compared with in-situ data and plume  
 42 theory. Vent temperatures reach 300°C, but anything transported by the plumes would  
 43 only experience these extreme conditions for very short times. This suggests that hydrother-  
 44 mal plumes may carry biological material, such as larvae, without causing harm. We also  
 45 studied how vent conditions affect plume behavior, focusing on its transition from the  
 46 source-dominated region to the turbulent region farther away, where it aligns with the  
 47 established theory. The transition zone shows behaviors crucial for interpreting seafloor  
 48 observations. Our findings provide new insights into how hydrothermal plumes behave  
 49 and interact with deep-sea environments.

50 **1 Introduction**

51 Unlike most of the abyssal plain, hydrothermal fields are oases of life and sites of  
 52 complex chemistry (Van Dover, 2002; Cotte et al., 2020), where hot fluids are discharged  
 53 through vents from chimney structures as black smokers, i.e., buoyant plumes. While  
 54 the total Earth's surface heat flux is typically  $\mathcal{O}(0.1 \text{ W m}^{-2})$  (Sclater et al., 1980; Davies  
 55 & Davies, 2010), hydrothermal plumes can generate heat fluxes of up to  $\mathcal{O}(1 \text{ GW m}^{-2})$   
 56 (Mittelstaedt et al., 2012). They play a significant role in the heat flux balance of hy-  
 57 drothermal fields (Barreyre et al., 2012; Mittelstaedt et al., 2012), influence faunal as-  
 58 semblages several meters away from fluid discharge points (Girard et al., 2020), and con-  
 59 tribute to the injection of dissolved iron and rare earth elements into the ocean (Chavagnac  
 60 et al., 2018).

61 Hydrothermal plumes typically rise several hundred meters (Lavelle et al., 2013;  
 62 Adams & Di Iorio, 2021) in the weakly stratified deep ocean, while vent radii are on the  
 63 order of centimeters. The discharged fluids reach temperatures of  $\sim 400^\circ\text{C}$  and fluid

64 velocities of up to  $\sim 1 \text{ m s}^{-1}$ , e.g., Koschinsky et al. (2008); Sarrazin et al. (2009), making  
 65 hydrothermal plumes an exotic phenomenon in contrast to typical ocean conditions.  
 66 Vent characteristics give rise to a wide range of plume behaviors, from jet-like plumes  
 67 (forced plumes) to highly buoyant plumes (lazy plumes). The great depths involved make  
 68 in-situ observations challenging, with data collection generally limited to the first few  
 69 meters above the source to attribute measurements to a specific vent cluster. Only re-  
 70 cent developments in acoustic imaging have efficiently captured hydrothermal system prop-  
 71 erties (Xu et al., 2013; Bemis et al., 2015).

72 Despite the importance of buoyant plumes in hydrothermal fields, few numerical  
 73 studies achieve resolutions that capture the physical processes at the scale of individual  
 74 vents. Most studies investigate plumes at much larger scales, assuming that the hot fluid  
 75 has already mixed with the environment and approximating the merging of vent fields  
 76 (Lavelle et al., 2013; Tao et al., 2013; Gao et al., 2019; Adams & Di Iorio, 2021). This  
 77 is largely due to the computational cost of achieving vent-scale resolution. Jiang and Breier  
 78 (2014), however, approached this level of detail using Reynolds-Averaged Navier-Stokes  
 79 (RANS) simulations, and showed that near-vent dynamics involve complex mixing pro-  
 80 cesses.

81 Morton et al. (1956) established a simplified theoretical model of plume dynam-  
 82 ics that successfully describes convective plumes in many situations (Kaye, 2008; Woods,  
 83 2010). The model parameterizes turbulence with the assumption that the entrainment  
 84 of surrounding fluid in the plume is proportional to its axial velocity. Dimensionless stud-  
 85 ies outside the hydrothermal regime, using Direct Numerical Simulation (DNS) by Plourde  
 86 et al. (2008); Taub et al. (2015); Marjanovic et al. (2017) and Large Eddy Simulation  
 87 (LES) by Devenish et al. (2010), have demonstrated that the classical assumptions of  
 88 the theoretical model do not hold in the near-field. In particular, forced or lazy plumes  
 89 with initial buoyancy transition to a purely buoyant – pure plume – regime (Van Reeuwijk  
 90 & Craske, 2015). The adjustment between the near-field and far-field hinders the appli-  
 91 cation of theoretical models (Ciriello & Hunt, 2020) and has been poorly characterized  
 92 for plumes, with even less attention given to the hydrothermal regime.

93 The aim of this paper is therefore to work within a realistic framework, specifically  
 94 in the hydrothermal regime. We focus on the near-vent region, which represents the win-  
 95 dow for in-situ operations and where black smokers interact with biochemical processes.  
 96 This makes the results directly applicable to the scale of hydrothermal fields.

97 In particular, due to their proximity to benthic communities, hydrothermal plumes  
 98 may serve as a mechanism for the vertical transport of larvae (Kim et al., 1994; Mullineaux  
 99 & France, 1995), influencing larval dispersal within the regional circulation (Xu et al.,  
 100 2018; Vic et al., 2018). However, no studies have focused on the near-vent region at high  
 101 resolution, particularly with regard to the influence of potentially lethal high temper-  
 102 atures on biotracers. This work aims to quantify the exposure time to high temperatures  
 103 in black smokers for a proxy tracer.

104 To address the near-vent physics of buoyant plumes with adequate resolution, we  
 105 use a Large Eddy Simulation (LES) approach with adaptive mesh refinement, which al-  
 106 lows centimeter-scale resolution within a 6 m domain above the vent. Specifically, we ex-  
 107 tensively study conditions encountered at the Lucky Strike hydrothermal vent field (north-  
 108 ern Mid-Atlantic Ridge), providing a realistic case study. This approach allows us to gain  
 109 new insights into the near-field hydrothermal regime, establish links with theoretical mod-  
 110 els, and explore the link between hydrothermal plumes and near-vent benthic commu-  
 111 nities.

112 The paper is organized as follows. Section 2 presents the governing equations and  
 113 details of the numerical experimental setup. Section 3 investigates the turbulent field of  
 114 a typical black smoker through its flow structure and compares it with the theoretical

model of Morton et al. (1956) and in-situ measurements. Section 4 extends the results to a wide range of source parameters to examine the flow field from forced to lazy plume. Section 5 discusses the impact of the transition regime on in-situ observations and the effect of temperature fluctuations on biotracer proxies. A summary of the results is given in section 6.

## 2 Model and Numerics

### 2.1 Plume Theory

The theory established by Morton et al. (1956) describes an axisymmetric Boussinesq plume with a radius  $r$  in a stratified fluid, with the assumption that the radial profiles of vertical velocity  $w$  and buoyancy  $b$  are similar at all heights. This model is hereafter referred to as the MTT model. This approach relies on a parameterization of mixing, the entrainment rate  $\alpha$ , which relates  $w$  at each height to the radial velocity  $e$  of the entrained water in the plume, such that  $\alpha = e/w$ .

The conservation of volume, momentum, and buoyancy flux, under these assumptions, yields the following equations:

$$\frac{d}{dz}(r^2w) = 2\alpha rw, \quad (1a)$$

$$\frac{d}{dz}(r^2w^2) = 2r^2b, \quad (1b)$$

$$\frac{d}{dz}(r^2wb) = 2r^2w\frac{g}{\rho_r}\frac{\partial\rho_a}{\partial z}, \quad (1c)$$

where  $\rho_a$  represents the ambient fluid density,  $\rho_r$  is a reference density, and  $g$  is the gravitational acceleration.

From the solutions of equations 1, the neutral buoyancy level  $H_{nbl}$  and the maximum height due to momentum overshoot  $H_{top}$  can be estimated as follows (Devenish et al., 2010):

$$H_{nbl} = 1.04 \alpha^{-1/2} B_0^{1/4} N^{-3/4}, \quad (2a)$$

$$H_{top} = 1.36 \alpha^{-1/2} B_0^{1/4} N^{-3/4}, \quad (2b)$$

where  $N$  is the buoyancy frequency, and  $B_0 = \pi r_0^2 w_0 b_0$  is the buoyancy flux at the source, with  $z = 0$  denoted by the subscript 0. The momentum flux and vertical volume flow are defined as  $M_0 = \pi r_0^2 w_0^2$  and  $Q_0 = \pi r_0^2 w_0$ , respectively.

In most cases, hydrothermal plumes carry momentum from the source, induced by subseafloor pressure. Morton and Middleton (1973) introduced two dimensionless parameters to characterize the balance of forces, expressed as

$$\Gamma(z) = \frac{r(z)b(z)}{\alpha w(z)^2}, \quad (3a)$$

$$\Gamma(z)' = \frac{\alpha b(z)}{r(z)N^2}. \quad (3b)$$

At  $z = 0$ ,  $\Gamma_0$  and  $\Gamma'_0$  represent the plume source parameters. For  $\Gamma_0 < 1$  the plumes are forced (relative excess of momentum), and for  $\Gamma_0 > 1$  the plumes are lazy (relative excess of buoyancy). When  $\Gamma'_0 \ll 1$ , the plume is rapidly balanced by the ambient stratification. The a priori choice of  $\alpha$  affects the  $\Gamma_0$  level and plume classification near  $\Gamma_0 = 1$ . Taub et al. (2015) noted that this dependence can cause inconsistencies between theory and observations.

The value of  $\alpha$  remains a subject of debate. The generally accepted values are 0.12 for buoyant plumes and 0.076 for pure jets (Woods, 2010; Kaye, 2008; Van Reeuwijk &

149 Craske, 2015; Richardson & Hunt, 2022). However, recent studies show that  $\alpha$  can vary  
 150 greatly in the near-field (Van Reeuwijk et al., 2016; Marjanovic et al., 2017). We assume  
 151 a fixed value of  $\alpha = 0.12$  for application to equations 1, 2, and 3.

## 152 2.2 Basilisk

153 Basilisk (Popinet, 2013) is an Adaptive Mesh Refinement (AMR) code that uses  
 154 an octree structure to discretize the computational domain. This approach provides re-  
 155 fined resolution in regions with small-scale features, while coarsening the grid in quies-  
 156 cent areas. The dynamic refinement adapts the mesh on the fly, efficiently focusing com-  
 157 putational effort on turbulent regions, making it well suited for plume studies. We set  
 158 the resolution so that the maximum resolution is  $d_{max} = 2.49$  cm to spatially resolve  
 159 the vent outlet, while the minimum resolution is set to  $d_{min} = 20$  cm. The code uses  
 160 a LES approach with a second-order accurate finite-volume solver for the Navier-Stokes  
 161 equations (Popinet, 2003, 2009, 2015). The equations are solved using the Boussinesq  
 162 and incompressibility assumptions, expressed as

$$\frac{\partial \mathbf{u}}{\partial t} + \nabla \cdot (\mathbf{u} \otimes \mathbf{u}) = \frac{1}{\rho_r} (-\nabla p + \nabla \cdot \mathbf{T}) + b \nabla z, \quad (4a)$$

$$\nabla \cdot \mathbf{u} = 0, \quad (4b)$$

163 where  $\mathbf{u}$  is the filtered velocity and  $z$  is the height above the source. The buoyancy is  
 164 defined as  $b = -g(\rho(x, t) - \rho_r)/\rho_r$ , where  $\rho(x, t)$  is the density at position  $x$  and time  
 165  $t$ . The model pressure  $p$ , representing the deviation from the hydrostatic reference pres-  
 166 sure  $P$ , is computed using a multigrid Poisson solver. Temperature  $T$  is integrated as  
 167 a conservative tracer using the robust upwind advection scheme of Bell et al. (1989). Den-  
 168 sity is computed by an extension of the Equation Of State (EOS) beyond the oceanic  
 169 funnel, namely for  $T > 40$  °C (see below). The stress tensor  $\mathbf{T}$  accounts for unresolved  
 170 small-scale turbulence. The Vreman (2004) sub-grid scale model is used to compute the  
 171 local eddy viscosity. This model requires a coefficient  $c$ , set to  $3.6 \times 10^{-2}$ , to allow a fair  
 172 chance for turbulent shear flow. The turbulent Prandtl number is set to unity, which im-  
 173 plies equal heat diffusivity and viscosity.

174 The Boussinesq approximation may seem questionable due to the large tempera-  
 175 ture anomalies at the vent, where the source temperature in this study is typically around  
 176  $T_0 = 300$  °C ( $\rho_0 = 782$  kg m<sup>-3</sup>) and the ambient temperature is  $T_a = 4.6$  °C ( $\rho_a =$   
 177  $1035$  kg m<sup>-3</sup>). However, the plume mixes rapidly as it exits (see section 3). At 25 cm  
 178 above the source, the average temperature drops to  $T = 50$  °C ( $\rho = 1021$  kg m<sup>-3</sup>), cor-  
 179 responding to an average density fluctuation of 1.4 % with respect to the reference den-  
 180 sity. At  $z = 1$  m, the mean temperature is close to  $T = 10$  °C, corresponding to a fluc-  
 181 tuation of 1 %, and temperatures of  $T > 40$  °C ( $\rho < 1025$  kg m<sup>-3</sup>) make up only 40  
 182 % of the distribution (Figure 2-e). Furthermore, the buoyancy flux is preserved in this  
 183 approximation. Thus, the introduced error is not expected to have a significant effect  
 184 on our results.

## 185 2.3 Equation Of State

186 An accurate EOS is needed for the 4–300 °C temperature range, at the hydrostatic  
 187 pressure of our target site, which is  $P \sim 1700$  dbar. TEOS-10 (IOC et al., 2010) is the  
 188 standard for computing seawater thermodynamics but is only valid in the oceanic fun-  
 189 nel, i.e.  $T < 40$  °C at 2000 m (McDougall et al., 2003). We need to extend the EOS  
 190 for temperatures above this range. Previous work by Sun et al. (2008) established a set  
 191 of fitted polynomial equations in the 4–300 °C range by combining freshwater and sea-  
 192 water data. A more recent study by Safarov et al. (2009), based on in-situ measurements  
 193 at  $S_A = 35.17$  g kg<sup>-1</sup>, covers the entire 0–195 °C range up to 1400 dbar with improved  
 194 accuracy. Bischoff and Rosenbauer (1985) determined the EOS for  $S_A = 32.16$  g kg<sup>-1</sup>  
 195 for the 200–350 °C range and up to 1000 dbar. To simplify the model, and due to a lack

of sufficient data, we neglect the specific chemistry of black smokers and assume a uniform absolute salinity of  $S_A = 35.2 \text{ g kg}^{-1}$ . To develop a smooth EOS that closely matches these published results, we developed a non-linear parametric fit covering the temperature and pressure range 0–350 °C and 1500–1700 dbar, typical of the conditions at Lucky Strike (Figure A1). To balance the salinity differences, the data from Sun et al. (2008) and Bischoff and Rosenbauer (1985) are adjusted based on TEOS-10 at  $S_A = 35.2 \text{ g kg}^{-1}$ . The corresponding correlation is given in Appendix A by equation A1.

#### 2.4 Outlet Turbulence Parameterization

The discrete sources observed at Lucky Strike systematically exhibit turbulence at the vent, which is expected due to the complex and irregular subsurface circulation that hot fluids undergo before reaching the seafloor (Fontaine et al., 2014). However, without numerical adjustments, the plume initially develops as a transitional laminar flow (Figure 1-a) until it destabilizes into a turbulent plume. This is an unrealistic feature that is corrected using the method of Plourde et al. (2008). To trigger turbulence in the plume, a uniform discrete white noise is added to the vertical velocity at all outlet nodes (Figure 1-b, experiment 1 in Table 1), such that  $w = w_0(1 + AW(t))$ , where  $W(t)$  is a white noise signal, and  $A$  is the noise amplitude. This parameterization represents the turbulence pre-existing in the flow prior to injection into the water column and fully accounts for the turbulent state at the outlet. The calculations show that for disturbance magnitudes  $A = [0–2]$ , the level of turbulence can be increased while keeping the plume numerically stable. However, a burst of viscous dissipation  $\varepsilon_k$  in the first nodes above the outlet limits the maximum energy that can be injected at the source. Therefore, we choose the optimal value of  $A = 0.5$ , which allows turbulence to develop quickly after the outlet while minimizing the burst in  $\varepsilon_k$ .

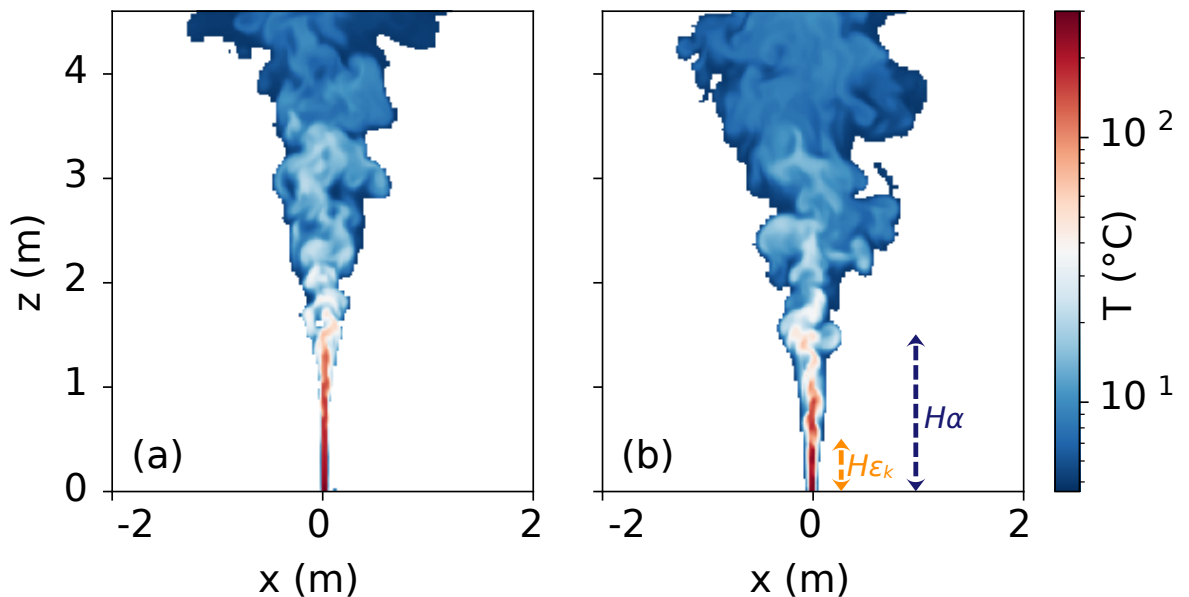


**Figure 1.** Cross-section of the instantaneous temperature field for (a) the scenario without noise perturbation at the outlet ( $A = 0$ ), and (b) with turbulence triggered by noise immediately after the outlet ( $A = 0.5$ ). The two reported heights correspond to the transition region to a pure plume regime (see section 4).

220      **2.5 Experiment Setup and Modeling Case**

221      The Tour Eiffel vent field (-1690 m) located at the Lucky Strike hydrothermal site  
 222      ( $37^{\circ}17'N$   $32^{\circ}16'W$ ) is selected as the baseline modeling case. It features a prominent 15  
 223      m high chimney with approximately 10 vents (Mittelstaedt et al., 2012) and is consid-  
 224      ered a biological hotspot (Van Audenhaege et al., 2022). We define a hydrothermal ed-  
 225      ifice as the collection of chimneys and complex topography resulting from hydrothermal  
 226      activity. Usual structures are smaller than Tour Eiffel, typically  $\sim 1\text{--}2$  m in height (Barreyre  
 227      et al., 2014).

228      Hydrothermal fluid exits the seafloor through two types of sources: diffuse low tem-  
 229      perature sources ( $T < 10$  °C), which are a mixture of hydrothermal fluid and ambient  
 230      water, and discrete high temperature sources, typically black smokers (Barreyre et al.,  
 231      2014). We focus on the plumes emitted by the latter. The EMSO-Açores (European Mu-  
 232      ltidisciplinary Subsea Observatory) long-term observatory, maintained through the Mo-  
 233      MARSAT campaign series, provides the framework for in-situ measurements.

234      The model domain is a cubic box of width  $L = 6.375$  m with open boundary con-  
 235      ditions on all sides, except for a solid flat bottom. To avoid boundary effects, results are  
 236      presented excluding regions near the boundaries. The plume is forced by imposing a tem-  
 237      perature  $T_0$  and vertical velocity  $w_0$  at the vent, modeled as an outlet with radius  $r_0$ .  
 238      A solid pipe was tested as a small chimney model to raise the outlet 1 meter above the  
 239      seafloor to allow more effective entrainment of the surrounding fluid. Simulation results  
 240      showed no significant differences, so for simplicity the outlet is kept at the bottom bound-  
 241      ary. The ambient stratification is linear in the vertical, with  $N = 1.63 \times 10^{-3}$  s $^{-1}$ , de-  
 242      termined from observations at Lucky Strike. The ambient temperature at the outlet is  
 243       $T_a = 4.6$  °C.

244      The diversity of source conditions is large, ranging from highly forced plumes to  
 245      highly lazy plumes. To capture this variability, the study examines a number of key pa-  
 246      rameters:  $r_0$  (1.4–2.8 cm),  $w_0$  (0.02–1.4 m s $^{-1}$ ), and  $T_0$  (40–340 °C). The selected range  
 247      for these parameters is based on field data collected by Mittelstaedt et al. (2012) at Tour  
 248      Eiffel. The experimental parameters are summarized in Table 1.

**Table 1.** Summary of simulations. The experiments are grouped based on common varying factors. The numerical domain size is  $L_0 = 6.375$  m. The maximum resolution is the same across all simulations ( $d_{max} = 2.49$  cm).

Experiment	Symbol	$w_0$ (m s $^{-1}$ )	$r_0$ (cm)	$T_0$ (°C)	$B_0$ (m $^4$ s $^{-3}$ )	$\Gamma_0$
1, 2, 3	■, ▲, ♦	0.7	2.8	[300, 100, 200]	[4.15e-3, 7.12e-4, 2.14e-3]	[1.1, 0.2, 0.6]
4, 5, 6	+ ×,	[1.4, 0.7, 0.4]	[1.4, 2.0, 2.8]	300	2.08e-3	[0.1, 0.8, 4.6]
7, 8	×, ▶	[1.4, 0.1]	2.8	300	[8.30e-3, 2.97e-4]	[0.3, 224]
9, 10, 11	★, ●, ▲	0.5	[1.4, 2.0, 2.8]	300	[7.41e-4, 1.48e-3, 2.97e-3]	[1.1, 1.6, 2.2]
12, 13	◆, ●	[0.05, 0.2]	1.4	300	[7.41e-5, 2.97e-4]	[112, 7.0]
14, 15	▲, ●	[0.05, 1.4]	2.8	40	[1.13e-5, 3.16e-4]	[8.5, 0.01]
16, 17	-, ★	[0.05, 1.12]	[1.4, 2.8]	200	[3.82e-5, 3.42e-3]	[58, 0.23]
18	▼	0.02	2.8	340	1.61e-4	1897

249      **2.6 Averaged Diagnostics**

250      To synthesize the LES results, diagnostic quantities are averaged both in time and  
 251      horizontally to provide vertical profiles. Horizontal averaging is performed within the plume,

which requires the definition of the plume boundary relative to the ambient. This definition is not straightforward and there is no generally accepted approach in the literature. Few attempts have been made to provide a precise definition (Pham et al., 2005; Plourde et al., 2008).

In this study, we define the plume boundary based on  $w$ : the plume interior is where  $|w| > \sigma$ . The typical value used is  $\sigma = 10^{-2} \text{ m s}^{-1}$ , determined by sensitivity tests, with any deviations specified. This criterion filters velocities between 1% and 10% of the axial values and is consistent with Morton et al. (1956)'s definition of the theoretical plume radius. We have verified that this criterion accurately captures the plume boundary for all source parameters in this study.

We define  $r(z, t)$  as the equivalent radius of the area  $S(z, t)$ , where  $S(z, t)$  is the plume cross-sectional area used for horizontal averaging. On average,  $S(z, t)$  corresponds to a disc, but this is not true for snapshot times, as turbulence causes the plume boundary to become convoluted. The profiles are time-averaged over the integration time ( $\sim 10$  min plume time) with an output every 1.5 s.

The entrainment rate is a key quantity from the LES and is obtained by  $\alpha(z, t) = e(z, t)/w(z, t)$ , where  $e(z, t)$  is the lateral flux entering the plume and  $w(z, t)$  is the mean vertical velocity. It is computed using

$$e(z, t) = \frac{1}{2\pi r(z, t)} \frac{d}{dz}(wS), \quad (5a)$$

$$w(z, t) = \frac{1}{S(z, t)} \int_{S(z, t)} w dS. \quad (5b)$$

### 3 Model Result for a Black Smoker

The aim of this section is to describe the near-field plume dynamics, to investigate the flow structure as a function of the entrainment rate, and to compare these results with those predicted by the MTT theoretical model and in-situ data.

#### 3.1 Mean Field

The experiment presented here represents a typical source at the Lucky Strike field (experiment 1 of Table 1). The regime is weakly lazy ( $\Gamma_0 = 1.14$ ), and as noted in section 2.1, the choice of  $\alpha$  affects the value of  $\Gamma_0$ . Its turbulent flow is more similar to a forced plume regime (see section 3.3), and the term forced plume is used for Experiment 1. We present the mean quantities averaged with  $\sigma = 1 \text{ cm s}^{-1}$  in Figure 2, together with the 95th percentile mean to highlight the upper range of the data distribution. Positive and negative spatial standard deviations are shown separately.

The high value of  $\Gamma'_0 = 4 \times 10^6$  reflects the strong injection of  $B_0$  into a weak stratification. The plume exits with an extremely high temperature anomaly ( $T - T_a \approx 300^\circ\text{C}$ ) and intense momentum forcing ( $w_0^2 = 0.5 \text{ m}^2 \text{ s}^{-2}$ ), significantly different from typical ocean conditions. It results in  $H_{nbl} \approx 3400 r_0$  according to the MTT model (see below), underscoring the focus on near-field behavior within this study ( $L_0 \approx 230 r_0$ ). However, the plume quickly converges to a more tempered state within the numerical domain, typical of the scale of hydrothermal edifices.

The mean temperature drops sharply from  $T_0 = 300^\circ\text{C}$  at the vent to less than  $T = 6.5^\circ\text{C}$  at  $z = 4 \text{ m}$ , and then follows a slower decay rate (Figure 2-b). Within the first meter, the temperature drops below  $T = 15^\circ\text{C}$ . Despite this rapid decrease, the region near the vent retains significantly high mean temperatures. The mean vertical velocity goes from  $w_0 = 70 \text{ cm s}^{-1}$  to  $w = 7 \text{ cm s}^{-1}$  within the first meter (Figure 2-c).  $w$  remains almost constant above this, with only a 10% variation between  $z = 1 \text{ m}$  and

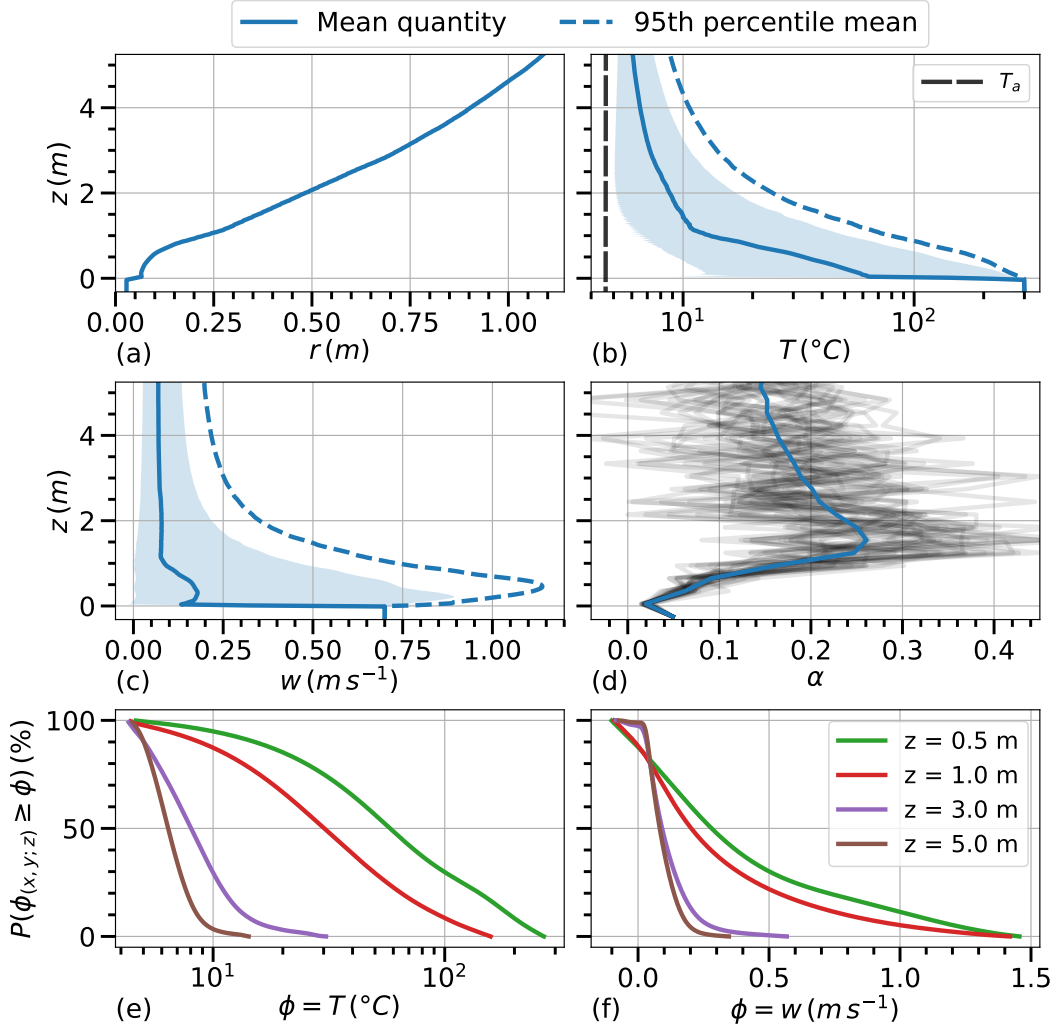


**Figure 2.** Vertical profiles for the time averaged (a) radius, (b) temperature, and (c) vertical velocity. (b)  $T_a$  is the ambient temperature (4.6 °C). The dashed line represents the 95th percentile mean (core plume), and the shaded region indicates the asymmetric spatial standard deviation. (d) Evolution of the entrainment rate  $\alpha(z)$  and its temporal variability. Complementary cumulative density function for (e) temperature and (f) vertical velocity at different heights above the source.

295  $z = 5$  m. The first meter is characterized by fluid acceleration, with the plume core reaching  
 296 a peak velocity of  $w = 1.14 \text{ m s}^{-1}$  at  $z = 0.5$  m, as discussed further below. The  
 297 radius increases linearly, indicating a constant spreading rate, reaching  $r = 1.05$  m at  
 298  $z = 5$  m. The area of averaging includes the boundary of the plume where most of the  
 299 mixing occurs. The averages are therefore sensitive to these regions of very low values,  
 300 which contribute to the sharp decreases in key variables and the rapid expansion observed  
 301 immediately after the outlet in Figure 2-a.

302 The plume dynamics observed in Figure 2, notably the stabilization of  $T$  and  $w$  pro-  
 303 files to nearly constant values, represent the adjustment between the near-field and far-  
 304 field regions. The entrainment of ambient water is necessary to dissipate the large val-  
 305 ues of  $T_0$  and  $w_0$  through mixing. This is reflected in the rapid increase in radius, which  
 306 grows by a factor of 37 between the vent and a height of  $z = 5$  m. This can be consid-  
 307 ered the dilution factor of the hydrothermal fluid (Figure 2-a). Coupled with the ver-  
 308 tical velocity, this results in a significant volume flow of  $Q = 0.25 \text{ m}^3 \text{s}^{-1}$  at  $z = 5$  m.  
 309 Thus,  $Q$  grows by a factor of 145 over a height of  $z \approx 200 r_0$ , highlighting the efficiency  
 310 of buoyancy-driven entrainment.

311 The weak stratification has no significant effect in the near-field. It was included  
 312 in the LES setup to make the simulation more realistic and to avoid unnecessary assump-  
 313 tions about the surrounding fluid. However, LES runs under the same conditions as Ex-  
 314 periment 1, but with a uniform ambient, give identical results for the vertical profiles of  
 315 the mean quantities. Nevertheless, the parameter  $N$  is crucial for explaining the plume  
 316 equilibrium level and cannot be ignored in larger numerical domains. According to the  
 317 MTT model, the neutral buoyancy level and maximum height are predicted to be  $H_{nbl} =$   
 318  $94$  m and  $H_{top} = 123$  m, respectively (equations 2-a, b). The solution of the MTT equa-  
 319 tions in uniform versus stratified environments begins to diverge at  $z \approx 0.4H_{nbl}$ . Here,  
 320 the numerical domain represents  $0.07H_{nbl}$ , which seems to be a reasonable limit for as-  
 321 suming a uniform environment, without accumulating significant errors.

### 322 3.2 Spatial Fluctuations

323 The rapid drop in mean temperature does not mean that the hot water is imme-  
 324 diately and completely mixed. Mixing takes some time. The 95th percentile distribu-  
 325 tion is assumed to represent the core of the plume. In this region, the temperature is sig-  
 326 nificantly higher than at the plume's edge (Figure 2-b), where ambient cold water is drawn  
 327 in and subsequently mixed.

328 To understand the mixing process, we present the Complementary Cumulative Den-  
 329 sity Function (CCDF) for temperature at different heights above the source (Figure 2-  
 330 e). The CCDF shows the probability of finding a parcel at height  $z$  with a temperature  
 331 greater than  $T$ . For example, at  $z = 1$  m, 50 % of the parcels have temperatures above  
 332  $30^\circ\text{C}$ , and 10 % exceed  $100^\circ\text{C}$ , while the mean temperature is only  $10^\circ\text{C}$ . This provides  
 333 information beyond the predictions of the MTT model and is valuable for understand-  
 334 ing chemical processes and larval dispersal. Implications for biological particles are dis-  
 335 cussed in section 5.2. At  $z = 3$  m, the maximum observed temperature is  $30^\circ\text{C}$ .

336 We apply the same diagnostic to the vertical velocity (Figure 2-f). Two points stand  
 337 out. First, local velocities can reach up to twice the exit velocity (up to  $1.5 \text{ m s}^{-1}$ ) be-  
 338 low  $z = 1$  m. Second, downward velocities occur within the plume, although with low  
 339 probability. The latter is directly related to the twisting vortical structures and their as-  
 340 sociated circulations (Figure 3). The first property shows that the core of the plume is  
 341 being accelerated. This acceleration is driven by buoyancy, with the available potential  
 342 energy carried by the hot water acting as a source of kinetic energy (Winters et al., 1995;  
 343 Wykes et al., 2015). Figure 2-c clearly shows that the vent buoyancy provides a local  
 344 acceleration of the core plume, strong enough to influence the mean value. The fluid ac-  
 345 celeration means that any in-situ measurement must take this effect into account, as es-

346 estimating the vent volume flow just centimeters above the source could lead to significant  
 347 errors.

348 The distribution of large anomalies in  $T$  and  $w$  remains significant within the first  
 349 meter. Due to the high temperature of the core being mixed, a specific extension of the  
 350 TEOS-10 EOS is still required 1 m above the vent. This highlights that the assumption  
 351 of a homogenized fluid based on mean quantities, with low  $w$  and  $T$  values for  $z < 3$   
 352 m, is incorrect. However, mixing drastically changes the balance of forces, subsequently  
 353 slowing the vertical motion and reducing the variance in the plume quantities  $w$  and  $T$ .  
 354 Beyond this region ( $z > 3$  m) the distributions of  $T$  and  $w$  show reduced spatial vari-  
 355 ation, which explains the slower decrease of their profiles and their convergence to nearly  
 356 constant values. At  $z = 5$  m, the absolute spread of  $T$  and  $w$  decreases to 10 °C and  
 357 0.34 m s<sup>-1</sup>, with a lower probability of extreme values, compared to an absolute spread  
 358 of 155 °C and 1.4 m s<sup>-1</sup> at  $z = 1$  m.

359 A key result is that the flow structure must be carefully considered in experiments  
 360 that initiate simulations at a dilute point above the vent, as many hydrothermal plume  
 361 simulations rely on this approach (Lavelle et al., 2013; Gao et al., 2019; Adams & Di Io-  
 362 rio, 2021). Approximating a uniform source below  $z = 5$  m fails to capture the dynam-  
 363 ics of the near-vent flow structure. In particular, the velocity fluctuations indicate that  
 364 turbulence is fully developed, and the plume cannot be assumed to be laminar in the near-  
 365 field.

### 366 3.3 Entrainment and Flow Structure

367 The entrainment rate,  $\alpha(z, t)$ , shows strong vertical and temporal variability, as-  
 368 sociated with intense mixing and the plume dilution. The overall value in the domain  
 369 is  $\alpha = 0.19$ , but it shows a vertical dependence with three distinct zones, consistent with  
 370 previous results obtained using DNS by Van Reeuwijk et al. (2016). For  $z < 0.7$  m, the  
 371 forced plume is driven by the source condition. The entrainment rate is similar to that  
 372 of a jet-like plume,  $\alpha = 0.07$ . This region corresponds to most in-situ observation ca-  
 373 pabilities. Between  $1 \text{ m} < z < 2 \text{ m}$ , the entrainment rate reaches its maximum ( $\alpha =$   
 374 0.26), which is twice the commonly accepted value for buoyant plumes. This entrainment  
 375 rate reflects intense mixing with cold fluid, contributing to the plume spreading, as well  
 376 as the dilution and homogenization of the temperature anomaly distribution. Buoyancy  
 377 driving the flow weakens, resulting in deceleration. For  $z > 3$  m, the entrainment rate  
 378 converges to a more conventional value ( $\alpha = 0.15$ ) for a pure plume (Van Reeuwijk &  
 379 Craske, 2015; Richardson & Hunt, 2022). This suggests that the plume reaches a self-  
 380 similar state, marking the end of the near-field transition regime (discussed in more de-  
 381 tail in section 4). This transition, as previously noted, is associated with an abrupt change  
 382 in the key variables  $T$  and  $w$  for  $z > 2$  m, with both converging to a weaker vertical  
 383 decay rate (Figure 2-b, c). The dilution process is responsible for the dissipation of the  
 384 large buoyancy flux  $B_0$  at the source.

385 The  $\alpha(z)$  profile is closely related to the turbulence field, which consists of differ-  
 386 ent scales of coherent structures. These structures can be observed using the  $\lambda_2$  tech-  
 387 nique (Jeong & Hussain, 1995), as shown in Figure 3. A real-time sequence of the tur-  
 388 bulent field observed with this technique is provided by the authors (Lemaréchal et al.,  
 389 2024a). The jet-like entrainment rate close to the source ( $z < 0.7$  m) is associated with  
 390 an unstable shear layer that forms ring vortices along the plume axis, typical of jet-like  
 391 flow. As the entrainment rate increases with height ( $z < 1.5$  m), the flow field becomes  
 392 turbulent. The vortices destabilize and break down into a helical mode, as described by  
 393 Fiedler (1988). The large, well-organized vortex structures between 1 m and 2 m, pre-  
 394 dominantly aligned in the horizontal plane, entrain more fluid than the smaller, less or-  
 395 ganized vortices that appear further downstream. This explains the maximum value of  
 396  $\alpha(z)$  observed at this height. This marks the transition region, where both the kinetic

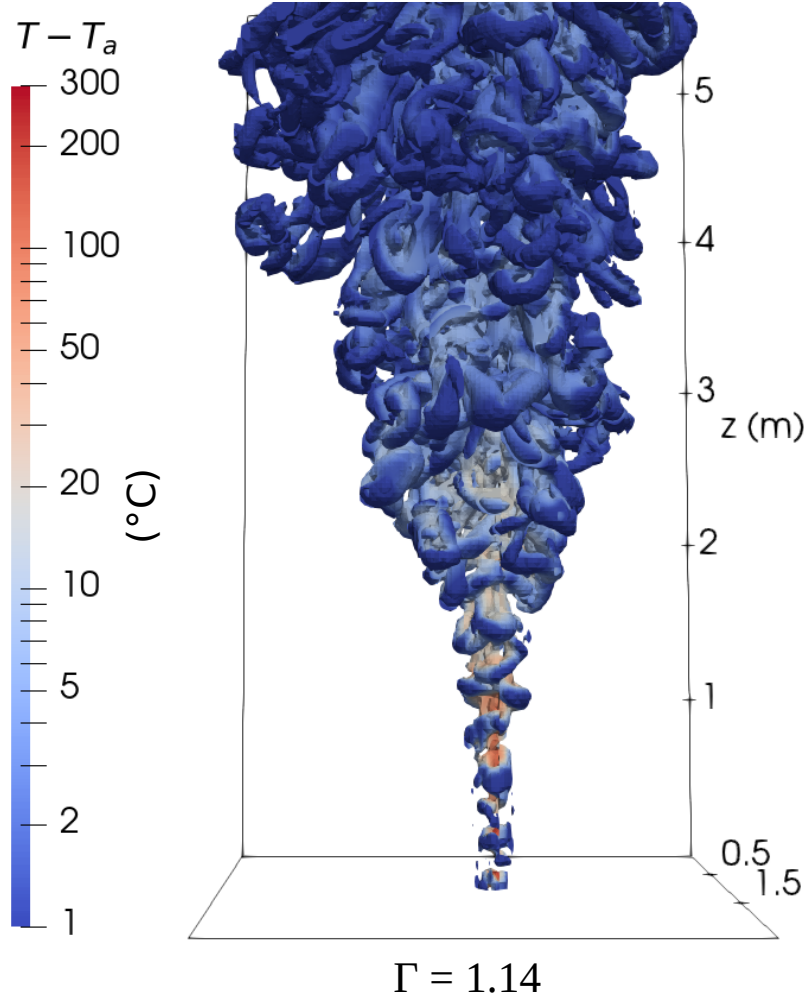


**Figure 3.** Three-dimensional coherent structures are visualized using the  $\lambda_2$  method (Jeong & Hussain, 1995) for iso-surfaces at  $\lambda_2 = -0.1$  for a plume near the forced plume regime (experiment 1). The colormap represents the temperature anomaly, with  $T_a = 4.6$  °C.

397 energy dissipation and the entrainment rate reach their peak. Beyond  $z = 1.5$  m, the  
 398 entrainment rate decreases as the flow enters a fully 3D convective turbulent state (pure  
 399 plume). The plume structure directly influences the entrainment rate and the energy dis-  
 400 sipation dynamics.

401 The instantaneous entrainment rate profiles (Figure 2-d – black lines) show signif-  
 402 icant temporal variability.  $\alpha(z, t)$  reaches a value of 0.5 at  $z = 1.6$  m, representing a  
 403 90% deviation from the mean. This observation adds to the evidence for strong mixing  
 404 in the vicinity of the vent. Similar behavior has been observed in experimental studies  
 405 (Matulka et al., 2014) and DNS studies (Plourde et al., 2008; Marjanovic et al., 2017).  
 406 We observe the same pattern in the hydrothermal regime. The temporal variability re-  
 407 sults from large-scale vortical structures driving the turbulent flow, as highlighted by Plourde  
 408 et al. (2008). Most of the entrainment occurs at the plume’s edge, while the core remains  
 409 less sensitive to mixing. Negative entrainment, up to  $\alpha = -0.06$ , is associated with de-  
 410 trainment processes reflected in the local downward velocities. This is associated with  
 411 the expulsion of fluid from the plume due to coherent turbulent structures. The influ-  
 412 ence of this mechanism on the mean field becomes noticeable only after  $z = 3$  m. Plourde

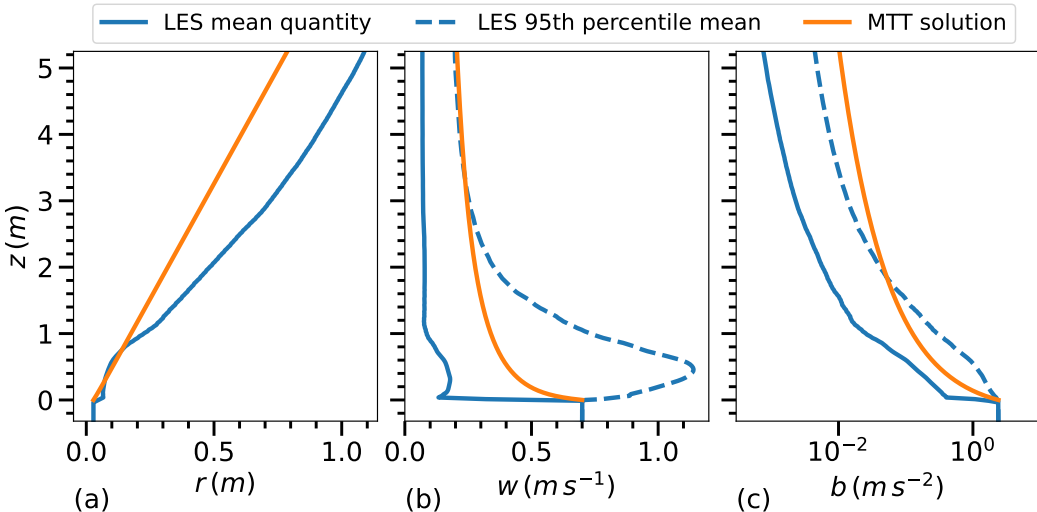


**Figure 4.** Vertical profiles of the flow field compared to the results obtained with the MTT model (1956) for its governing parameters: (a) radius, (b) vertical velocity, and (c) buoyancy. The dashed line represents the 95th percentile mean of the LES results (core plume).

et al. (2008), using higher resolution DNS, identified it as an expulsion and contraction mechanism of local coherent structures driving the dominant entrainment process.

### 3.4 Comparison with the MTT Model

LES mean quantities can be compared with predictions from integral models. Figure 4 compares LES data with the MTT model predictions, the most widely used theoretical model. It shows that the self-similar conservation equations derived by Morton et al. (1956) do not hold in the near-field. The MTT equations in Figure 4-a, b, c capture the general trend of the flow field but do not agree well with the mean profiles. This discrepancy cannot be attributed to horizontal averaging choices, as the MTT model best represents the core plume evolution for  $z > 2$  m. At  $z = 5$  m, the radius predicted by the MTT model is 30 % smaller, and the difference in the velocity profiles results in  $Q = 0.37 \text{ m}^3 \text{ s}^{-1}$ , which is 30 % higher than the LES flow field.

In particular, the fluid acceleration contradicts the self-similarity assumption in the MTT model, which predicts a monotonic decrease in vertical flow velocity (Figure 4-b). This was shown by Marjanovic et al. (2017) for lazy plumes. Here, we show that the buoyancy flux injected by black smokers in a forced plume regime is sufficient to induce the same effect.

A virtual origin correction can be applied to the source to account for the point source assumption of the MTT model (Hunt & Kaye, 2001). However, the length  $L_q = 5Q_0/(6\alpha M_0^{1/2})$ , which represents the distance from the actual source to the virtual source of a pure plume (Hunt & Kaye, 2005), has little effect on the results ( $L_q = 29$  cm) and is therefore not applied.

The adjustment between the vent conditions and an ordered far-field flow, corresponding to a pure plume regime, is responsible for the breakdown of the self-similarity assumption. This prevents the direct application of the theoretical model. This is in agreement with recent findings by Matulka et al. (2014); Van Reeuwijk et al. (2016); Marjanovic et al. (2017); Ciriello and Hunt (2020) and highlights the need for analytical solutions

adapted to this region. This adjustment to the far-field occurs through mixing, which is reflected in the strong variability of the  $\alpha(z, t)$  profile. Thus, our work confirms the main limitation of the MTT model: the entrainment rate cannot be assumed constant in the transition region between the near-field and far-field. It shows that although theoretical models are often used to calibrate measurement techniques (Crone et al., 2008; Mittelstaedt et al., 2012), near-field hydrothermal plume predictions cannot rely solely on these models.

Another approach to measuring the entrainment rate is to derive  $\alpha$  from the spreading rate, represented by the local derivative  $\partial z / \partial r$  and expressed as the angle  $\hat{\beta}$  between the plume boundary and the horizontal. Plumes do not always maintain a constant spreading rate, particularly in cases of necking in lazy plumes (Marjanovic et al., 2017). Here, however, the radius shows a steady increase, corresponding to a nearly constant angle  $\hat{\beta} = 84^\circ$ . The spreading rate is linked to the MTT assumptions through  $\alpha$ . Applying  $\hat{\beta}$  to the conservation of volume in the MTT model gives a theoretical value of  $\alpha = 0.10$ .

Two key points can be made. First, the spreading rate remains nearly constant in the near-field for hydrothermal plumes. This is consistent with the assumption of the model developed by Priestley and Ball (1955), which is related to the MTT model (Fox, 1970). Secondly, the derived value of  $\alpha = 0.10$  is close to the classical one (Richardson & Hunt, 2022), while the mean value  $\alpha = 0.19$ , obtained through direct computation, is almost twice as high due to the turbulent field in the near-vent region. This shows that while black smokers can be captured to some extent by integral models, these models fail to reproduce the detailed dynamics observed near the vent.

### 3.5 Comparison to In-Situ Observations

Here, we assess how accurate our model is compared to direct measurements. Reproducing black smokers in laboratory experiments is technically challenging (Shabbir & George, 1994; Crone et al., 2008), while accessing hydrothermal fields at depth presents its own set of challenges. Our LES results are compared with in-situ data from the MoMARSAT2023 cruise using Remotely Operated Vehicle (ROV) operations.

The in-situ experimental setup is shown in Figure 5. Sampling was performed at a typical source in the Tour Eiffel field. The vertical observation window,  $H_{obs}$ , is limited to 60 cm above the vent. The key parameters to be retrieved are the plume radius and the temperature profile. The optical width, i.e., the visible gradient density anomalies, provides a measure of the apparent radius of the plume, although this measure is subject to perspective distortion. Radius measurements are based on video recordings with a reference scale, consisting of 300 frames and a step size of  $dz_{obs} \approx 5\% H_{obs}$ . The temperature profile is measured with a probe positioned along the plume centerline above the vent, with  $dz_{obs} \approx 10\% H_{obs}$  and a sampling rate of 1 Hz. Horizontal currents were negligible during the experiment.

The in-situ data are compared with the LES equivalent in Figure 6 (experiment 9 of Table 1). The values of  $r_0 = 1.4$  cm and  $T_0 = 300$  °C for the LES experiment are chosen based on the in-situ measurements at  $z = 0$  m. The Root Mean Squared (RMS) value is used to represent the temporal dispersion of the in-situ data.

The vertical velocity at the source is a complicated parameter to measure accurately using only video data (Crone et al., 2008; Mittelstaedt et al., 2012). First,  $\sigma$  is set to 10 cm s<sup>-1</sup>, which captures the plume contour effectively measurable in videos. For any given set of source parameters tested, a smaller  $\sigma$  value includes density gradients too weak to be detected visually in the video, as well as colder parcels. This causes an incoherent sharp increase and decrease in  $r$  and  $T$ , respectively, immediately after the exit (Figure 6-a, b). Then,  $w_0$  is estimated based on LES experiments. Several experiments are run with the same  $r_0$  and  $T_0$  values as above, to determine the  $w_0$  value that gives a ra-

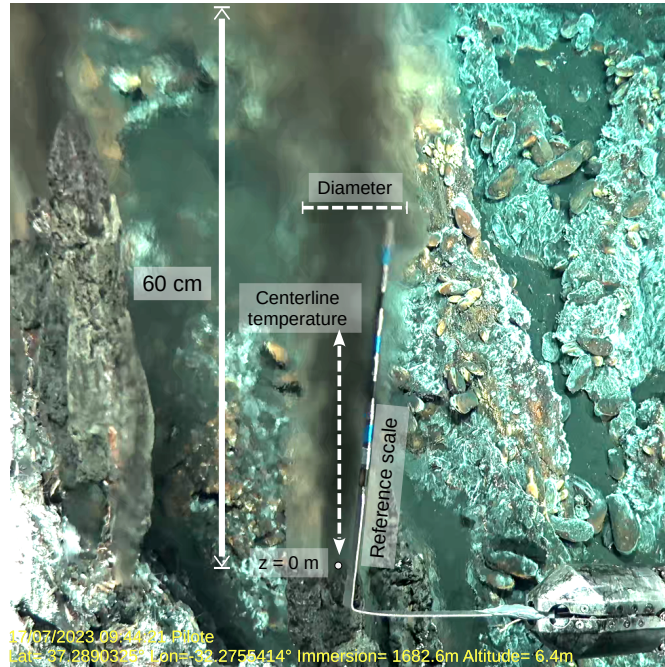


**Figure 5.** Photograph of the plume and schematic of the parameters used to measure the temperature and diameter of the plume. The reference scale gives the pixel-to-real distance ratio. Height above the source is measured from the reference point at  $z = 0$  m. Diameter is measured by identifying the visible outer edges of the plume relative to the surroundings. Temperature is measured along the centerline of the plume.

490 dius and temperature profile that best matches the in-situ data. It is found to be  $w_0 =$   
491  $0.5 \text{ m s}^{-1}$ .

492 The LES radius and temperature profiles are in good agreement with the exper-  
493 imental data. The variability of the in-situ radius at  $z_0$  reflects the temporal evolution  
494 of the effective equivalent surface through which the flow passes. In fact, the vent ge-  
495 ometry does not resemble a well-defined pipe, but consists of closely spaced sources, each  
496 less than a centimeter wide, which together form a single plume exit. The RMS of the  
497 in-situ data increases with height as the plume moves and bends away from its axis, in-  
498 trroducing a bias from the 2D view of the apparent radius, which is not captured by the  
499 LES method of calculating  $r$ .

500 The LES plume is slightly colder at the source, but this does not significantly af-  
501 fect the profiles. The LES experiment accurately reproduces the rapid decrease from 220  
502 °C at  $z = 5 \text{ cm}$  to 85 °C at  $z = 30 \text{ cm}$ . The blue dots in Figure 6-b represent the pro-  
503 file expected from LES for a thermal sensor placed on the axis. Due to the stirring ef-  
504 fect of turbulent structures, the mean profile along the axis is interchangeable with the  
505 temperature averaged over a slice bounded by  $\sigma = 50 \text{ cm s}^{-1}$ . This indicates that  $w$   
506 measurements on the axis are expected to be larger than this  $\sigma$  value.

507 The in-situ profile deviates from the LES profile for two reasons. In practice, the  
508 sensor is not perfectly centered, resulting in a colder in-situ profile. The in-situ profiles  
509 correspond better to the mean LES profile for the area bounded by  $\sigma = 10 \text{ cm s}^{-1}$ . Sec-  
510 ond, the thermal inertia of the instrument misses the parcels with the highest fluid tem-  
511 peratures, such as rapidly ascending turbulent structures, as shown by the small RMS  
512 of the field data compared to the LES spatial variability.

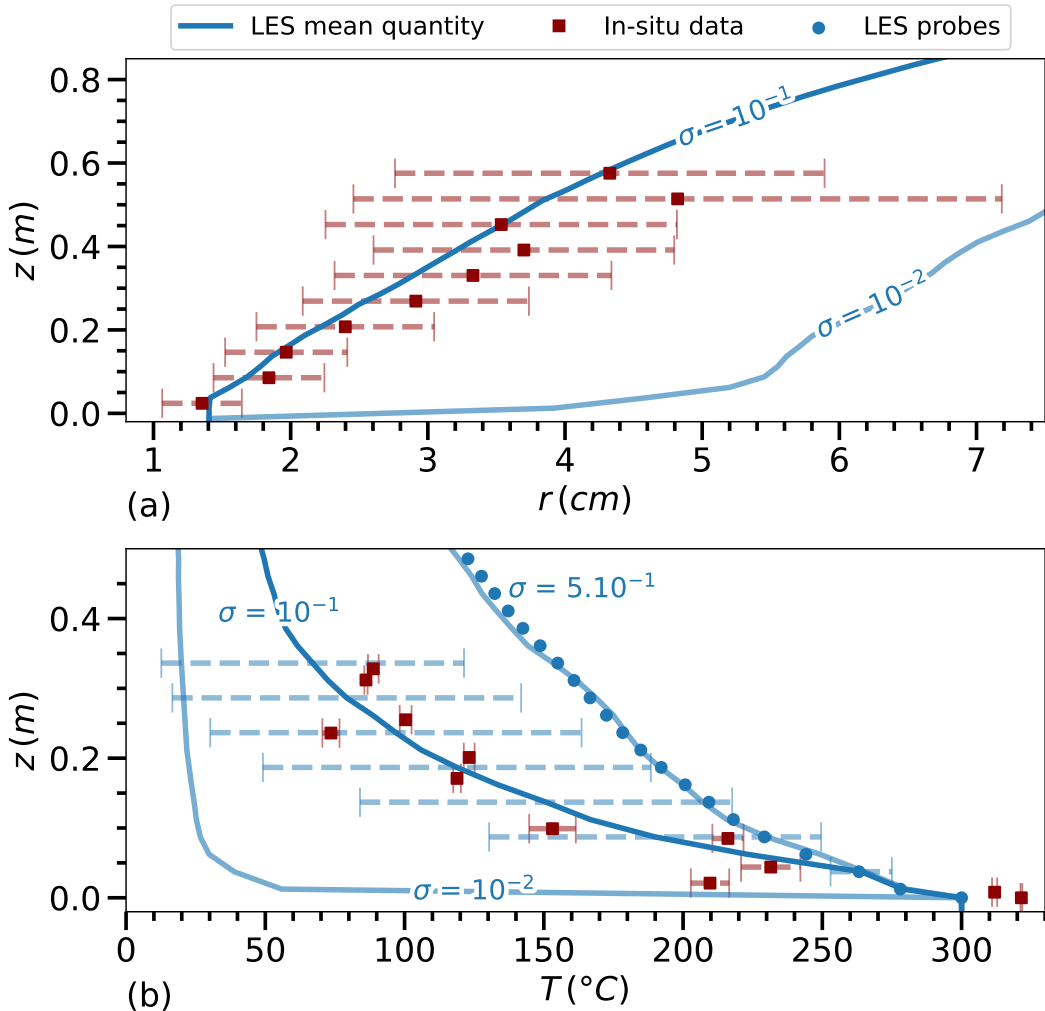


**Figure 6.** Profiles of (a) the plume radius and (b) temperature for the in-situ data and the LES mean quantities for different values of  $\sigma$  (in  $m s^{-1}$ ). The blue dots represent numerical probes indicating the time-averaged temperature at the plume axis. The error bars represent the spatial RMS for the LES data and the temporal RMS for the in-situ data.

513      The consistency of the LES and in-situ radius and temperature profiles for  $H_{obs} =$   
 514      60 cm gives us confidence in the reliability of the LES model in the near-vent region, in  
 515      contrast to the MTT model. In addition, the good agreement close to the source vali-  
 516      dates the parameterization of the vent turbulence.

## 517      4 Sensitivity to Source Parameters

518      Hydrothermal plumes can exist under a wide range of conditions, from forced to  
 519      lazy plume regimes. In this section, we extend the results to a large set of vent source  
 520      parameters. We provide a detailed description of the transition region from the near-vent  
 521      to the pure plume regime. The resulting flow field adjustments are analyzed on the ba-  
 522      sis of plume theory. We use experiments 1 to 18 (Table 1), for which the set of condi-  
 523      tions is summarized in Figure 7-a, covering most of the parameter space of hydrother-  
 524      mal vents.

### 525      4.1 Transition Region

526      As the plume mixes with the ambient fluid, the potential energy of the density anomaly  
 527      decreases, and a fraction of it is converted into momentum through the buoyancy flux  
 528      (Wykes et al., 2015). Therefore, assessing the transition height  $H_t$  based on the ratio of  
 529      forces using the  $\Gamma(z)$  parameter becomes complicated because the momentum combines  
 530      with the kinetic energy resulting from buoyancy. Indeed, several studies have shown that  
 531       $\Gamma(z)$  exhibits complex behavior before converging to 1 (Hargreaves et al., 2012; Taub et  
 532      al., 2015; Marjanovic et al., 2017), and its dependence on  $\alpha$  further complicates the task.

533      To address this issue, we frame the transition region using two indicative heights.  
 534      The first height,  $H_{\varepsilon_k}$ , corresponds to the location of maximum viscous dissipation, ex-  
 535      cluding the peak associated with noise injection. A consistent pattern in the vertical pro-  
 536      file of viscous dissipation is observed across all results, showing an increase that culmi-  
 537      nates in a peak within the first meter. This point indicates the establishment of a bal-  
 538      ance between the shear generated by the injection of momentum and the buoyancy force.  
 539      The second height,  $H_\alpha$ , marks the location where the maximum entrainment of ambi-  
 540      ent water occurs, indicating the complete destabilization of the plume column into 3D  
 541      turbulence. As noted by Taub et al. (2015); Marjanovic et al. (2017),  $\alpha(z)$  converges to  
 542      a constant in the self-similar state. These heights are illustrated in Figure 1-b.

543      Figure 7-b shows the rapid horizontal expansion in the transition region for a highly  
 544      lazy plume (S1 - experiment 12), a plume in balance (S2 - experiment 9), and a forced  
 545      plume (S3 - experiment 7).  $H_{\varepsilon_k}$  and  $H_\alpha$  effectively capture the transition from vertical  
 546      streamlines to a turbulent field (Figure 3) and frame the maximum of the derivative  $d \log(r^2/r_*^2)/dz$ ,  
 547      where  $r_*$  is a reference radius. In Figure 7-c, the heights  $H_{\varepsilon_k}$  and  $H_\alpha$  are plotted against  
 548      the parameter  $\Gamma_0$ . Two key points emerge.

549      Despite a 6 order of magnitude variation in  $\Gamma_0$ , the transition region exhibits rel-  
 550      atively small amplitude changes ( $\Delta H_{\varepsilon_k} = 0.5$  m and  $\Delta H_\alpha = 0.95$  m). This shows that  
 551      the transition region remains almost invariant to the set of parameters  $r_0$ ,  $w_0$  and  $b_0$  en-  
 552      countered at the hydrothermal site.  $H_\alpha$  ranges from 1.20 m to 2.15 m, and  $H_{\varepsilon_k}$  ranges  
 553      from 0.25 m to 0.75 m, with S1 and S3 differing by a factor of only 1.7. However, a sim-  
 554      ilar trend emerges for both heights  $H_{\varepsilon_k}$  and  $H_\alpha$ . The transition region extends further  
 555      away from the source as  $\Gamma_0$  increases. This is consistent with the results of Taub et al.  
 556      (2015), whose analysis of entrainment rate profiles suggests that lazy plumes reach self-  
 557      similarity further away from the source than forced plumes.

558      Forced plumes – up to  $\Gamma_0 = 1$  – driven by momentum flux are unstable, charac-  
 559      terized by intense shear leading to rapid destabilization of the column ( $H_{\varepsilon_k} \approx 0.3$  m  
 560      for  $\Gamma_0 < 1$ ). When the source buoyancy flux balances the input momentum, it slows

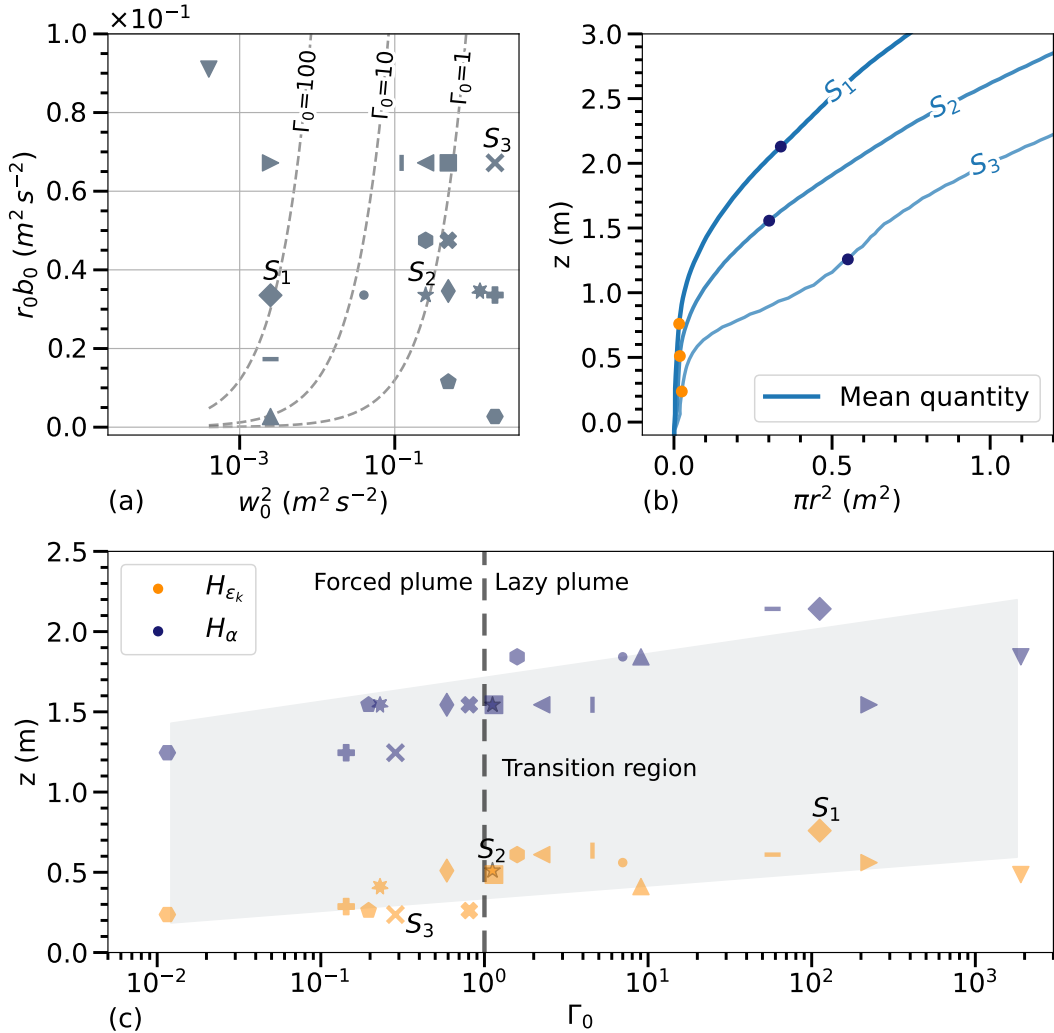


**Figure 7.** (a) Ratio of input buoyancy-radius product to momentum for experiments 1 to 18. (b) The surface of horizontal expansion for three different source conditions, with their transition heights defined by  $H_{\varepsilon_k}$  (in orange) and  $H_\alpha$  (in blue). (c) Transition heights as a function of  $\Gamma_0$ , the plume source parameter. The dashed line separates the forced and lazy plume regimes, while the grey area encompasses the plume's transitional state.

561 the development of convective turbulence compared to jet-like plumes ( $H_{\varepsilon_k} \approx 0.5$  m  
 562 for  $\Gamma_0 = 1$ ). In all cases, the flow requires a minimum height of  $H_\alpha \approx 1.2$  m to fully  
 563 develop convective turbulence, even under a highly forced plume regime. It is worth noting  
 564 that the noise injected at the source accelerates the onset of turbulence.

565 The second consequence is that the transition region is not sharply delineated, as  
 566 it extends between  $H_{\varepsilon_k}$  and  $H_\alpha$ . The characteristic length scale,  $L_m = M_0^{3/4} B_0^{-1/2}$ , has  
 567 been proposed for forced plumes as the separation between jet-like and plume-like re-  
 568 gions by Morton (1959). A similar length scale for lazy plumes, marking the transition  
 569 to pure plume behavior, is  $L_a = Q_0^{3/5} B_0^{-1/5}$  (Hunt & Kaye, 2005). Recent studies by  
 570 Taub et al. (2015) and Wang and Law (2002) report  $z > 5 L_m$  or  $z > 6 L_m$  as the transi-  
 571 tion limit between jet-like and plume-like regions. However, these lengths do not ac-  
 572 curately represent the hydrothermal plume flow field. For  $\Gamma_0 < 1$ ,  $L_m \approx 18$  cm, and  
 573 the transition to the plume-like region occurs for  $z > 8 L_m$ , which is slightly higher but  
 574 still within reasonable agreement with the literature. In contrast,  $L_m$  increases for highly  
 575 forced plumes, which is not consistent with the trend observed for the LES. For  $\Gamma_0 >$   
 576 1,  $L_a \approx 4$  cm, but convergence to self-similarity clearly occurs at  $z > 40 L_a$ .

577 The high buoyancy flux involved may explain the limited relevance of both  $L_m$  and  
 578  $L_a$ . Our results support the definition of a relatively broad transition region, bounded  
 579 by  $H_{\varepsilon_k}$  and  $H_\alpha$ , above which the plume reaches a pure plume regime and below which  
 580 the source conditions dominate. This region is highlighted in grey in Figure 7-c, span-  
 581 ning from 0.25 m to 2.15 m, and is characteristic of hydrothermal vent conditions. For  
 582 simplicity, this region is referred to as  $H_t$  hereafter. The transition region corresponds  
 583 to the scale of hydrothermal edifices and falls within the range accessible by in-situ ob-  
 584 servational techniques, indicating that hydrothermal plumes observed near the seafloor  
 585 are typically in a transitional state.

586 Finally, the minimal effect of  $b_0$  and  $w_0$  on  $H_t$  suggests that other factors play a  
 587 more significant role.  $H_t$  is closely related to the vertical extent of the plume, with re-  
 588 sults showing  $H_t \approx H_{nbl}/100$ . While variations in  $r_0$  were limited due to small vent sizes  
 589 and could influence  $H_t$ , the parameter  $N$ , which was kept constant and is weak enough  
 590 to assume uniform ambient conditions, has a dominant effect on  $H_{nbl}$  due to its larger  
 591 scaling exponent in equation 2a. With realistic stratification,  $H_t$  remains less than 5%  
 592 of  $H_{nbl}$ , even for the experiment with the lowest  $B_0$  (experiment 14, where  $H_{nbl} = 21$   
 593 m from equation 2a). Thus, it is very likely that achieving a significant change in  $H_t$  would  
 594 require unrealistically high  $N$  values to reduce  $H_{nbl}$  to a scale comparable to the observed  
 595  $H_t$  for hydrothermal plumes.

## 596 4.2 Organization of the Flow Field

597 We focus on the relationships between the key flow variables in this transition re-  
 598 gion. Figure 8 presents the link between  $r$  and  $w$ , and  $b$  and  $w$  below ( $z = 0.29$  m) and  
 599 above ( $z = 5.0$  m) the transition height. Each experiment is related to its  $B_0$  value. Con-  
 600 sistent relationships indicate that the flow primarily depends on  $B_0$ . To limit spatial av-  
 601 eraging effects of cold fluid at the plume boundary, we restrict  $\sigma$  to  $10 \text{ cm s}^{-1}$ , which fil-  
 602 ters out experiments 12, 14, and 16 in Figure 8-b, d.

603 The organization is chaotic in the near-vent region, dominated by vent conditions  
 604 (Figure 8-a, c). In contrast, a clear organizational pattern emerges after reaching the pure  
 605 plume regime (Figure 8-b, d). The relationships between  $r$  and  $w$ , as well as  $b$  and  $w$ ,  
 606 both collapse to single power-law curves. Wang and Law (2002) showed that the mean  
 607 axial velocity and turbulent concentration fluctuations similarly collapse into Gaussian  
 608 curves for both forced and lazy plumes in pure plume regime.

609 In Figures 8-b and 8-d,  $B_0$  governs the overall organization of the flow, setting the  
 610 levels reached for each key variable above the transition region, where pure plume be-

611 behavior is observed. The pattern does not depend on the excess force at the source. Con-  
 612sequently, there are no scenarios where one quantity, such as  $w$ , becomes disproportio-  
 613nately large while others, such as  $r$  or  $b$ , remain small. Instead, the system organizes it-  
 614self to maintain consistency in the overall energy and momentum balance, with all vari-  
 615ables adjusting together to reflect the level of  $B_0$  injected.

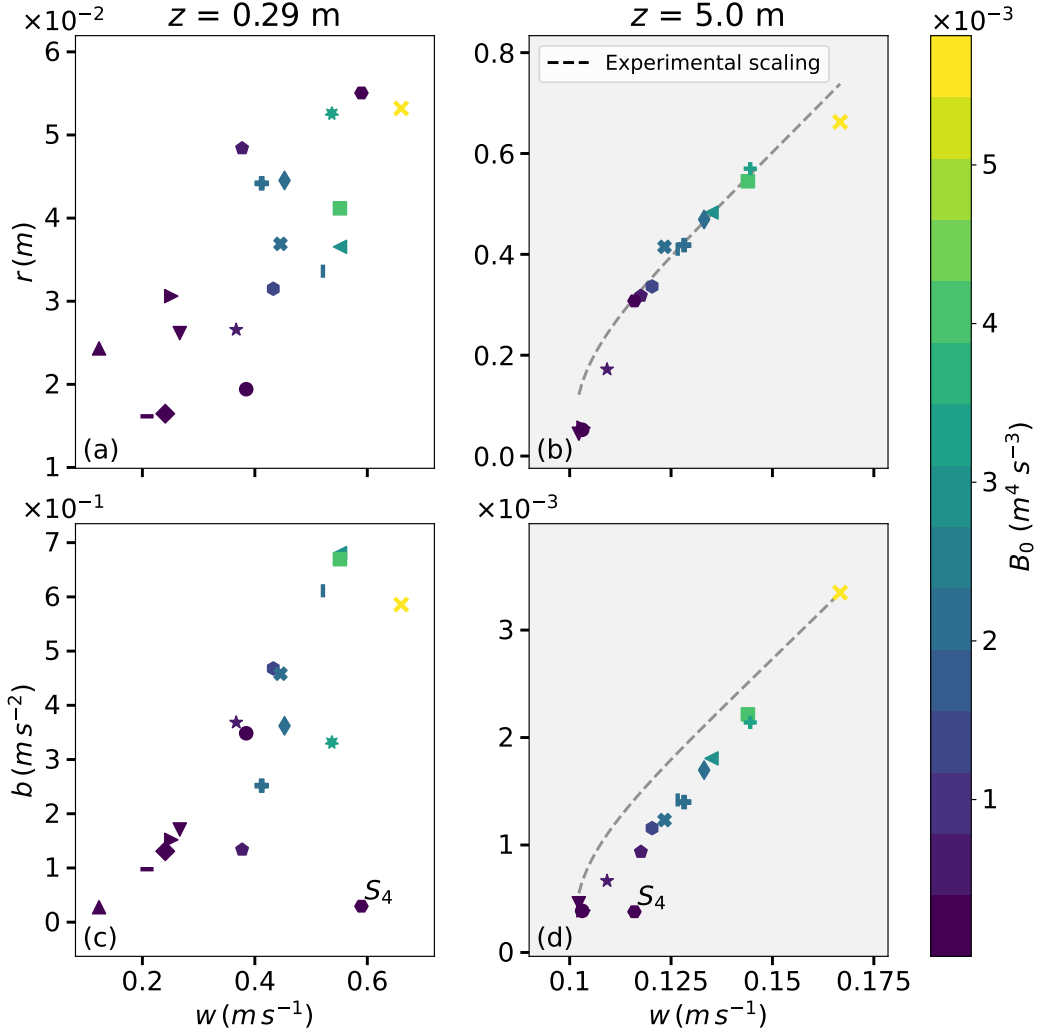


**Figure 8.** (a, b) Plume radius and (c, d) horizontal mean of buoyancy as a function of vertical velocity for  $\sigma = 10 \text{ cm s}^{-1}$ . Each experiment is shown (a, c) below and (b, d) above the transition region identified in section 4.1. The symbols are colored according to the source buoyancy flux. Experimental scalings are plotted from (b) equation 8 and (d) equation 7b.

616 This is consistent with the buoyancy flux conservation approach in the MTT equa-  
 617tions. The derivation of the theoretical model predicts an equilibrium level based solely  
 618 on  $B_0$  and the ambient stratification (equations 2). The scaling laws obtained from the  
 619 LES experiments reflect this behavior.

620 In a uniform environment, which is a valid assumption here (see section 3.1), the  
 621 right-hand term in equation 1-c vanishes, simplifying the MTT model to the analytical

622 solutions

$$r \propto z, \quad (6a)$$

$$b \propto B_0^{2/3} z^{-5/3}, \quad (6b)$$

$$w \propto B_0^{1/3} z^{-1/3}. \quad (6c)$$

623 These equations imply that the buoyancy flux is conserved at all heights. By combin-  
 624 ing them, the relationships between the key plume variables are derived

$$r \propto B_0^{-1/3} z^{4/3} w, \quad (7a)$$

$$b \propto B_0^{1/3} z^{-4/3} w. \quad (7b)$$

625 A custom factor  $C_1(z) = 2.81 z^{-0.74}$  is applied to equation 7b to account for empiri-  
 626 cal deviations observed in the flow field data, resulting in the scaling shown in Figure 8-  
 627 d. It agrees within 20% with the factor predicted by Morton et al. (1956).

628 The agreement with the scaling laws improves with height as the distance from the  
 629 transition region increases, indicating a breakdown of self-similarity in this region. Typ-  
 630 ically, for plumes with  $\Gamma_0 \ll 0$ , such as solution S4 ( $\Gamma_0 = 0.01$  - experiment 15), equa-  
 631 tion 7b incorrectly predicts high values of  $b$  for high values of  $w$ . Only when the highly  
 632 forced plume dissipates its input momentum does it converge to the solution predicted  
 633 by the scaling (Figure 8-c, d). However, even at  $z = 5$  m, the relationship between  $b$   
 634 and  $w$  has not fully collapsed to the self-similarity solution. Taub et al. (2015) suggests  
 635 that buoyancy fluctuations are influenced by source conditions over a longer range than  
 636 velocity fluctuations.

637 Equation 6a shows the limitations of the analytical solution based on the assump-  
 638 tion of a uniform environment. In this case, the plume radius is predicted to be inde-  
 639 pendent of  $B_0$ , leading to an inconsistent relationship between  $r$ ,  $w$ , and  $B_0$  in equation 7a.  
 640 In particular, increasing values of  $B_0$  result in decreasing plume radius for the analyt-  
 641 ical solution, which is not consistent with the LES flow field. This discrepancy with the  
 642 MTT model is due to its assumption of a constant spreading rate between plumes. The  
 643 deviation observed in our results indicates a difference in the spreading rates, which is  
 644 consistent with the experimental results of Kitamura and Sumita (2011). They observe  
 645 that pure jets have a slightly higher spreading rate than plumes; however, this difference  
 646 is generally considered to be small (Kotsovinos & List, 1977; Van Reeuwijk et al., 2016).

647 To align the scaling in equation 7a with the LES flow field, the dependence on  $B_0$   
 648 is adjusted, and an empirical correction factor  $C_2(z)$  is introduced. This modified scal-  
 649 ing is expressed as

$$r = C_2(z) B_0^{1/3} z^{4/3} w, \quad (8)$$

650 where  $C_2(z) = -0.27z + 3.9$ . This adjustment results in the scaling shown in Figure 8-  
 651 b.

652 The overall agreement between the scaling and the LES experiments shows that,  
 653 despite the strong influence of the near-vent region on the flow, the turbulent field can  
 654 be simplified by scaling laws as plume quantities converge toward self-similarity. This  
 655 indicates that in the far-field the MTT model captures the underlying physics based on  
 656 the  $B_0$  value. The LES results highlight that  $B_0$  is the main controlling parameter, even  
 657 in the exotic hydrothermal regime where high buoyancy flux is injected into weak strat-  
 658 ification.

659 

## 5 Discussion

660 

### 5.1 Transition Region Observation

661 The transition region between vent conditions and the pure plume region is identified  
 662 in an in-situ recording of a black smoker at the Tour Eiffel site. The video described  
 663 below was captured by a ROV and is provided by the authors (Lemaréchal & Matabos,  
 664 2023). The comparison is summarized in Figure 9. The source observed here is the same  
 665 as that used for the in-situ measurements in section 3.5, and experiment 9 is presented  
 666 as the numerical counterpart.

667 We focus first on observations near the seafloor (between 15:10 and 15:44 in the  
 668 video). The visible plume length is about 60 cm (Figure 9-b), while for this source,  $H_{\varepsilon_k} =$   
 669 0.51 m and  $H_\alpha = 1.53$  m. Compared to its numerical equivalent, this limits the analy-  
 670 sis to region (1) in Figure 9-a, which is dominated by vent conditions. As the ROV as-  
 671 cends (between 16:15 and 18:54), the camera transitions from focusing on the near-vent  
 672 region through the transition region (gray region labeled 2). At  $z \approx 2$  m, the camera  
 673 reaches the fully buoyant region of the plume (gray region labeled 3 – around 17:30), where  
 674 larger convective structures and fully three-dimensional turbulence dominate (accord-  
 675 ing to LES data we get  $r \approx 0.4$  m,  $w \approx 5$  cm s $^{-1}$ ). At this height, the mean temper-  
 676 ature ( $T \approx 7$  °C) and the density gradient anomalies associated with the refractive in-  
 677 dex gradient decrease drastically. The light reflection from plume particles becomes in-  
 678 sufficient to distinguish the plume clearly from its surroundings (e.g., at 17:50). In ad-  
 679 dition, the plume merges with those from neighboring sources, making numerical com-  
 680 parisons or in-situ studies of single source plumes extremely challenging.

681 Region (1) to (2) is the primary source of data for in-situ experiments, but this lim-  
 682 itation introduces a bias in our understanding of the plume dynamics. By restricting ob-  
 683 servations to this specific region, we capture a view of the plume that is limited to its  
 684 near-vent structure, which is strongly influenced by the transition from vent condition  
 685 to pure plume behavior, where scaling laws fail.

686 

### 5.2 Impact of Temperature Fluctuations on Tracer Proxies

687 Temperatures above 40°C have been documented as lethal to various organisms (Fisher,  
 688 1998; Bates et al., 2010; Lee et al., 2015). Given the high temperatures typical of black  
 689 smokers, biotracer survival during transport through the plume might be expected to  
 690 be unlikely. Consequently, studies often focus on stable environments that exclude such  
 691 high-temperature conditions, e.g., Lee et al. (2015). However, LES results suggest that  
 692 hydrothermal plumes could serve as a viable vector for biological material transport, as  
 693 prolonged exposure to high temperatures is unlikely.

694 Below, we estimate how long particles transported within the first three meters of  
 695 the rising plume are exposed to high and potentially lethal temperatures. To establish  
 696 a high-temperature threshold of interest, we use the 40 °C criterion, which represents a  
 697 reasonable estimate of the thermal tolerance limit for hydrothermal fauna. We distin-  
 698 guish between the plume’s inner core and its outer envelope, numerically defined as the  
 699 closest cells to the plume boundary. The LES experiment is chosen to reflect the source  
 700 conditions identified in section 3.5 (experiment 9 in Table 1). It provides an actual ex-  
 701 ample of a source in close proximity to a dense faunal community (Van Audenhaege et  
 702 al., 2022).

703 Due to computational limitations, an Eulerian approach was chosen over the ideal  
 704 Lagrangian method. Fixed probes serve as proxies for the trajectory of a particle entrained  
 705 in the plume. These probes are placed vertically at intervals corresponding to the mesh  
 706 resolution, either along the plume axis or at its boundary. The envelope probes are po-  
 707 sitioned at the intersection of the horizontal plane with the contour of the plume vol-

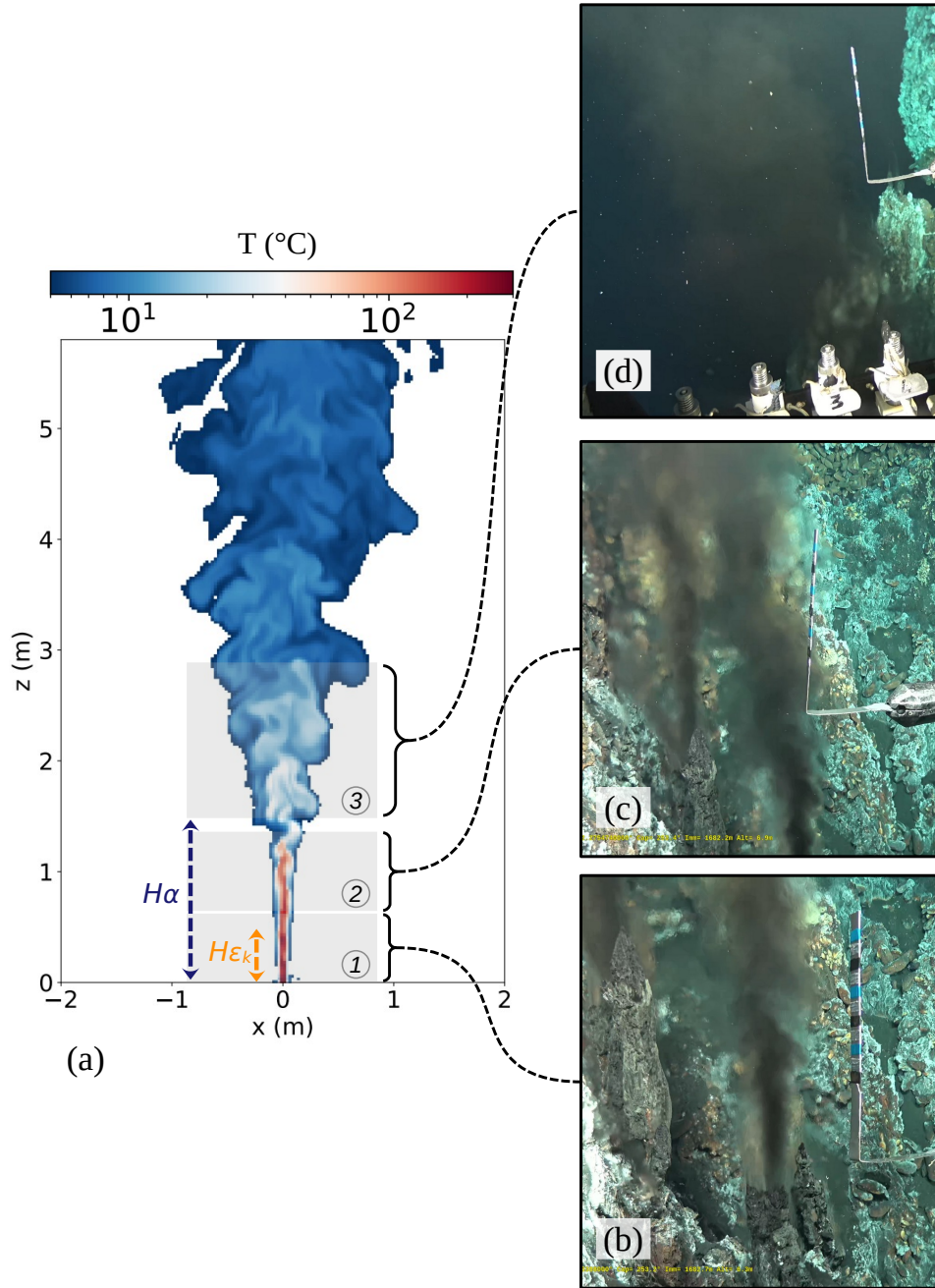


**Figure 9.** (a) Cross-sectional view of the instantaneous temperature field from a LES experiment (exp. 9), illustrating three types of regions corresponding to their respective in-situ observation windows as viewed during a video-recorded ROV exploration at Tour Eiffel. (b) The view corresponding to the height  $H_{\epsilon_k}$ , (c) the view corresponding to  $H_\alpha$ , and (d) the region where the plume reached its fully convective turbulent state.

708  
709  
710  
711  
712  
ume that satisfies the criterion  $\sigma = 0.1 \text{ m s}^{-1}$  on time average. This criterion is con-  
sistent with that used to match the in-situ data, and selects a plume region with suffi-  
cient vertical velocity to effectively advect materials. The bias introduced by sampling  
the plume with a 1D line of probes is mitigated by the large number of measurements  
taken over time: we use a sampling rate of 0.4 seconds over a duration of 14 minutes.

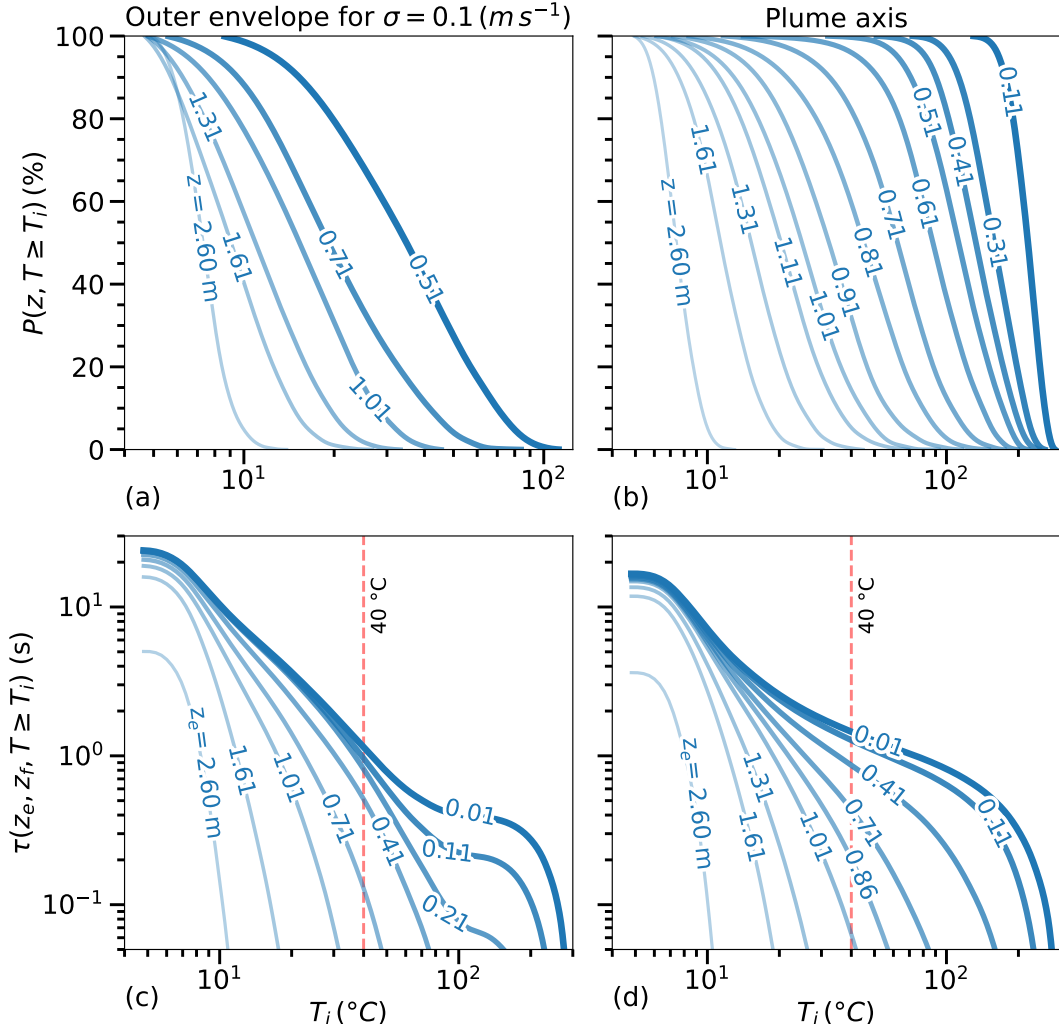


**Figure 10.** Complementary Cumulative Distribution Function (CCDF) of temperature at different heights  $z$  above the vent, for (a) the plume envelope selected by the criterion  $\sigma = 0.1 \text{ m s}^{-1}$  and (b) the plume axis. (c, d) The cumulative time  $\tau$  spent above each temperature  $T_i$  encountered in the hydrothermal fluid for trajectories along the vertical is shown in the same regions. Integration is performed for different starting entry heights  $z_e$  inside the plume up to  $z_f = 3 \text{ m}$ . (c, d) Plots are truncated below  $5 \times 10^{-2} \text{ s}$ .

713  
714  
715  
716  
Figure 10-a,b shows the CCDF,  $P(z, T \geq T_i)$ , derived from the time series of tem-  
perature at each fixed probe location. At  $z = 80 \text{ cm}$ , the plume axis shows  $T > 40$   
°C events representing 60 % of the time distribution, with a maximum temperature of  
150 °C at this height (Figure 10-b). These high temperatures disappear from the core

717 after 1.30 m. Within the envelope, it takes 1 m to eliminate temperatures above 40 °C.  
 718 At 70 cm, such temperatures occur 12 % of the time, peaking at 80 °C.

719 The probability distribution alone suggests that a tracer would encounter lethal  
 720 temperatures in both the core and the envelope of the plume within the first meter above  
 721 the vent. To investigate this further, we compute the cumulative time  $\tau$  (s). It is the time  
 722 taken by a parcel entering the plume at height  $z_e$  to reach height  $z_f$ , following the tra-  
 723 jectory traced by the 1D probe lines, with a temperature exceeding  $T_i$ . This computa-  
 724 tion is performed in the envelope (Figure 10-c) and along the plume axis (Figure 10-d).  
 725 The results are integrated from different starting entry heights  $z_e$  in the plume up to  $z_f =$   
 726 3 m, where the temperature has decreased significantly, according to

$$\tau(z_e, z_f, T \geq T_i) = \int_{z_e}^{z_f} \frac{P(z, T \geq T_i)}{w_p(z)} dz, \quad (9)$$

727 where  $w_p(z)$  is the vertical speed at the probe location. The maximum  $\tau$  for each curve  
 728 indicates the transit time between  $z_e$  and  $z_f$ .

729 The rationale for considering different starting heights  $z_e$  is that hydrothermal plumes  
 730 are often associated with complex local topography, where the fluid comes into contact,  
 731 providing different entry points for a tracer above the plume source. Below 30 cm, the  
 732 envelope and core become indistinguishable, resulting in a characteristic bump in the en-  
 733 velope curve, as the cumulative time reflects the core values (Figure 10-c), and  $w_p$  ex-  
 734 ceeds the value chosen for  $\sigma$  in this region.

735 In the envelope, below  $z_e = 40$  cm, exposure to temperatures above 40 °C lasts  
 736 for around 1 s, with significant exposure to higher temperatures, e.g., more than 0.3 s  
 737 above 70 °C for  $z_e = 11$  cm. For a particle entering at 41 cm, exposure to temperatures  
 738 above 40 °C lasts for 0.5 s, with only  $5 \times 10^{-2}$  s above 75 °C. Exposure to high temper-  
 739 atures decreases significantly above 70 cm. A trajectory along the axis experiences 0.9  
 740 s above 40 °C for  $z_e = 41$  cm, with a significant duration above very high temperatures  
 741 compared to the envelope, e.g., 0.25 s above 100 °C. High temperature exposure along  
 742 the plume axis becomes negligible only after 1 m. While particle paths are simplified for  
 743 practical purposes by considering 1D lines, it is important to note that particles could  
 744 be advected through both regions discussed, and it is essential to assess the viability of  
 745 tracers as a percentage of success. Nevertheless, both the core and the envelope of the  
 746 plume show minimal exposure to high temperatures for a particle entrained 1 m above  
 747 the vent. The envelope is a more favorable region for sustained transport for an entry  
 748 closer to the vent ( $z_e = 40$  cm), considering the temperature levels and time exposure  
 749 ratio, compared to the plume centerline.

750 These results support the findings of Kim et al. (1994), who demonstrated through  
 751 dye experiments and the MTT model that a single black smoker can enable substantial  
 752 vertical transport of larvae, opening pathways to habitats typically inaccessible to near-  
 753 bottom larvae.

## 754 6 Conclusions

755 Hydrothermal plumes inject a high buoyancy flux into weak stratification, rising  
 756 from centimeter-scale vents to heights of several hundred meters (Lavelle et al., 2013).  
 757 They play a key role in vent fields but have been poorly characterized in the near-vent  
 758 region. To study these plumes, we used a LES approach with adaptive mesh refinement  
 759 to achieve centimeter-scale resolution within a 6 m domain above the vent. Several key  
 760 points can be highlighted.

761 First, a typical black smoker (forced plume) is studied to quantify the mean flow  
 762 and spatial fluctuations, which are difficult to measure in deep-sea vent fields. The mean  
 763 temperature decreases sharply from  $T_0 = 300$  °C to  $T - T_a = 1.5$  °C at  $z = 5$  m, and

764 the velocity decreases from  $w_0 = 70 \text{ cm s}^{-1}$  to  $w = 7 \text{ cm s}^{-1}$ . This results in a sub-  
 765 substantial volume flow of  $Q = 0.25 \text{ m}^3 \text{s}^{-1}$  at  $z = 5 \text{ m}$ . The plume expands at a nearly  
 766 constant spreading rate. The results compare well with in-situ measurements. While lazy  
 767 plumes initially accelerate (Marjanovic et al., 2017), we show that forced plumes in the  
 768 hydrothermal regime also accelerate due to significant buoyancy, reaching  $w = 1.14 \text{ m}$   
 769  $\text{s}^{-1}$ . Numerical approaches to hydrothermal plumes often model a diluted point source  
 770 above the vent, e.g., Adams and Di Iorio (2021); however, approximating a uniform source  
 771 below  $z = 5 \text{ m}$  fails to capture the flow dynamics, especially since turbulence is fully  
 772 developed at this height.

773 Secondly, we show that the entrainment rate exhibits strong vertical and tempo-  
 774 ral variability, associated with the intense mixing required to dissipate the high source  
 775 buoyancy flux. The overall value in the near-field is  $\alpha = 0.19$ , which is significantly higher  
 776 than the classical value of  $\alpha = 0.12$  for a pure plume (Van Reeuwijk & Craske, 2015;  
 777 Richardson & Hunt, 2022). However, the values vary significantly in the vertical, from  
 778  $\alpha = 0.07$  in the jet-like plume region to  $\alpha = 0.15$  in the pure plume region, with much  
 779 larger values in between. The large variations in  $\alpha(z, t)$  are linked to the coherent struc-  
 780 tures of the turbulent field. Variations reaching up to 90% above the mean profile di-  
 781 lute and homogenize the temperature anomaly distribution, contributing to the flow de-  
 782 celeration. It highlights the main limitation of the MTT model (Morton et al., 1956):  
 783  $\alpha$  cannot be assumed constant in the near-field. A more appropriate approach would in-  
 784 incorporate the work of Wang and Law (2002), who developed a second-order integral model  
 785 to account for entrainment rate variations, where  $\alpha(z)$  is treated as a function of the lo-  
 786 cal Richardson number.

787 Extreme temperatures ( $T > 100 \text{ }^\circ\text{C}$ ) occur for  $z < 2 \text{ m}$ , coinciding with the abil-  
 788 ity of the plume to entrain biotracers from the seafloor. While the limited biological tol-  
 789 erance to high temperatures suggests that particle survival during transport through the  
 790 plume is unlikely, our study offers a different perspective. For a proxy tracer, exposure  
 791 times at  $T > 40 \text{ }^\circ\text{C}$  can be as short as 0.5 s in the plume envelope, depending on the  
 792 height of entrainment, decreasing to  $5 \times 10^{-2} \text{ s}$  above  $T = 75 \text{ }^\circ\text{C}$ . This challenges the  
 793 concept of lethal temperatures in dynamic flows. Hydrothermal plumes could thus act  
 794 as viable vectors for the transport of biological material from the seafloor, supporting  
 795 the findings of Kim et al. (1994), provided more is known about the ability of the fauna  
 796 to withstand such conditions for very short periods.

797 Finally, the sensitivity to source parameters is investigated for the forced and lazy  
 798 plume regimes. We show that the adjustment from the near-vent region, dominated by  
 799 source conditions, to the far-field, pure plume regime, leads to the breakdown of self-similar  
 800 plume behavior in this transition region. This prevents the application of the theore-  
 801 tical model of Morton et al. (1956) in the transition region, which extends from  $z = 0.25$   
 802 m to  $z = 2.15 \text{ m}$ . The transition height shows little sensitivity to the plume regime and  
 803 would require unrealistic changes in stratification to be significantly affected. Plumes ob-  
 804 served at the scale of hydrothermal edifices are typically in a transition state, which may  
 805 introduce bias into experimental studies at this depth. In the far-field, plumes converge  
 806 to self-similarity and can be described by scalings 7b and 8 derived from plume theory.  
 807 While the mean quantities do not agree well with the MTT model predictions, the flow  
 808 field in the pure plume region agrees with the MTT model approach and is primarily or-  
 809 ganized according to the source buoyancy flux.

## 810 Data Availability Statement

811 The real-time sequence of the turbulent field observed with the  $\lambda_2$  technique is avail-  
 812 able on Zenodo at <https://doi.org/10.5281/zenodo.13829868> (Lemaréchal et al., 2024a).  
 813 The in-situ recording of a black smoker can be accessed online in 720p resolution at <https://video.ifremer.fr/video?id=52548> and downloaded in 4K resolution on SEANOE at  
 814

815 <https://doi.org/10.17882/103869> (Lemaréchal & Matabos, 2023). A code to com-  
 816 pute the parametric EOS is available on Zenodo at [https://doi.org/10.5281/zenodo  
 817 .14332032](https://doi.org/10.5281/zenodo.14332032) (Lemaréchal et al., 2024b).

### 818 Acknowledgments

819 The authors acknowledge support from Université de Bretagne Occidentale, the iAtlantic  
 820 project (Grant #818123) supported by the European Union's Horizon 2020 (H2020) pro-  
 821 gram, the LOPS, and the Interdisciplinary Graduate School for the Blue Planet project  
 822 (ANR-17-EURE-0015). This work was performed using HPC resources from GENCI-  
 823 TGCC (Grant #2022-A0090112051). We warmly thank the crews of *L'Atalante* who par-  
 824 ticipated in the MoMARSAT cruises. We also acknowledge M. Matabos, P.-M. Sarradin,  
 825 and M. Cannat for co-leading and managing the MoMARSAT cruises and the EMSO-  
 826 Azores observatory.

## 827 Appendix A Parametric EOS

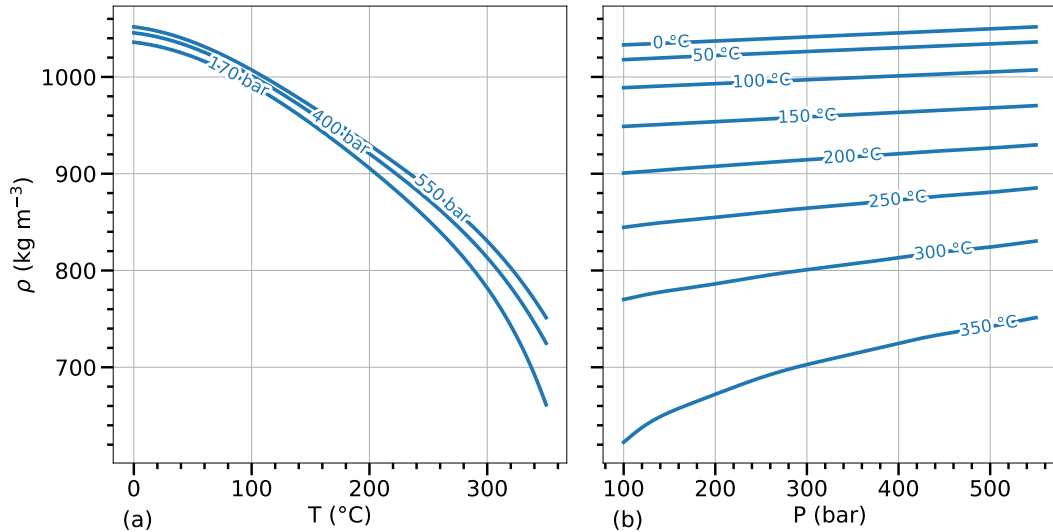


**Figure A1.** (a) Density of seawater vs. temperature calculated by equation A1 for different levels of pressure. (b) Density vs pressure for different levels of temperature.

828 This section presents the Equation Of State (EOS) developed for hydrothermal flu-  
 829 ids. The EOS is valid in the range of 100–550 bar and 0–350 °C at  $S_A = 35.2 \text{ g kg}^{-1}$ .  
 830 A plot of density for different pressure and temperature ranges is shown in Figure A1.

831 The density  $\rho$  (kg m<sup>-3</sup>) as a function of absolute temperature  $T$  (°C) and abso-  
 832 lute pressure  $P$  (bar) is given by

$$\rho(T, P) = A(P) \exp(-B(P)T) + C(P) + D(P) \exp\left(-\frac{(T - E(P))^2}{2F(P)^2}\right), \quad (\text{A1})$$

833 where  $A(P)$  ...  $F(P)$  are polynomials in  $P$  of the form

$$X(P) = \sum_{i=0}^8 c_i P^{8-i}, \quad (\text{A2})$$

834 with  $c_i$  being the polynomial coefficients given in Table A1 for each parameter. A code  
 835 sample to compute this equation is provided by the authors (Lemaréchal et al., 2024b).  
 836 To spare computing resources during calculations, we recommend generating an EOS ta-  
 837 ble with a fixed step for efficient data interpolation through array indexing.

**Table A1.** Polynomial coefficients of equation A2

	0	1	2	3	4	5	6	7	8
A	-7.01307390e-21	1.95660070e-17	-2.23352820e-14	1.30848310e-11	-3.97395990e-09	5.53535930e-07	-3.96405330e-05	1.37810860e-03	-1.62833820e-02
B	-2.04801770e-22	5.85654850e-19	-7.17814260e-16	4.93110400e-13	-2.08500570e-10	5.61590670e-08	-9.67436850e-06	1.04954760e-03	-7.55052580e-02
C	-9.08091870e-18	2.56711040e-14	-3.09991740e-11	2.08730680e-08	-8.57874330e-06	2.21278690e-03	-3.54404280e-01	3.36599270e+01	-7.59305030e+02
D	9.14772610e-18	-2.58613080e-14	3.12300980e-11	-2.10288630e-08	8.64259430e-06	-2.22918380e-03	3.57047310e-01	-3.38666710e+01	1.79999190e+03
E	-2.57551460e-19	7.36404340e-16	-9.02945380e-13	6.20751900e-10	-2.62358970e-07	7.01422040e-05	-1.17048000e-02	1.14665420e+00	-7.20442180e+01
F	2.80580730e-18	-7.95146740e-15	9.63263680e-12	-6.51411210e-09	2.69367930e-06	-7.01266430e-04	1.14048660e-01	-1.11301910e+01	7.25953200e+02

## 838 References

- 839 Adams, I., & Di Iorio, D. (2021). Turbulence properties of a deep-sea hydrothermal  
 840 plume in a time-variable cross-flow: Field and model comparisons for dante in  
 841 the main endeavour field. *Journal of Geophysical Research: Oceans*, 126(9),  
 842 e2020JC016638. doi: <https://doi.org/10.1029/2020JC016638>
- 843 Barreyre, T., Escartín, J., Garcia, R., Cannat, M., Mittelstaedt, E., & Prados, R.  
 844 (2012). Structure, temporal evolution, and heat flux estimates from the lucky  
 845 strike deep-sea hydrothermal field derived from seafloor image mosaics. *Geo-  
 846 chemistry, Geophysics, Geosystems*, 13(4). doi: <https://doi.org/10.1029/2011GC003990>
- 847 Barreyre, T., Escartín, J., Sohn, R. A., Cannat, M., Ballu, V., & Crawford, W. C.  
 848 (2014). Temporal variability and tidal modulation of hydrothermal exit-  
 849 fluid temperatures at the lucky strike deep-sea vent field, mid-atlantic ridge.  
 850 *Journal of Geophysical Research: Solid Earth*, 119(4), 2543–2566. doi:  
 851 <https://doi.org/10.1002/2013JB010478>
- 852 Bates, A. E., Lee, R. W., Tunnicliffe, V., & Lamare, M. D. (2010). Deep-sea hy-  
 853 drothermal vent animals seek cool fluids in a highly variable thermal envi-  
 854 ronment. *Nature Communications*, 1(1), 14. doi: <https://doi.org/10.1038/ncomms1014>
- 855 Bell, J. B., Colella, P., & Glaz, H. M. (1989). A second-order projection method for  
 856 the incompressible navier-stokes equations. *Journal of computational physics*,  
 857 85(2), 257–283. doi: [https://doi.org/10.1016/0021-9991\(89\)90151-4](https://doi.org/10.1016/0021-9991(89)90151-4)
- 858 Bemis, K. G., Silver, D., Xu, G., Light, R., Jackson, D., Jones, C., ... Liu, L.  
 859 (2015). The path to covis: A review of acoustic imaging of hydrothermal  
 860 flow regimes. *Deep Sea Research Part II: Topical Studies in Oceanography*,  
 861 121, 159–176. doi: <https://doi.org/10.1016/j.dsr2.2015.06.002>
- 862 Bischoff, J. L., & Rosenbauer, R. J. (1985). An empirical equation of state for hy-  
 863 drothermal seawater (3.2 percent nacl). *American Journal of Science*, 285(8),  
 864 725–763. doi: <https://doi.org/10.2475/ajs.285.8.725>
- 865 Chavagnac, V., Ali, H. S., Jeandel, C., Leleu, T., Desrigneville, C., Castillo,  
 866 A., ... others (2018). Sulfate minerals control dissolved rare earth ele-  
 867 ment flux and nd isotope signature of buoyant hydrothermal plume (emso-  
 868 azores, 37 n mid-atlantic ridge). *Chemical Geology*, 499, 111–125. doi:  
 869 <https://doi.org/10.1016/j.chemgeo.2018.09.021>
- 870 Ciriello, F., & Hunt, G. (2020). Analytical solutions and virtual origin cor-  
 871 rections for forced, pure and lazy turbulent plumes based on a univer-  
 872 sal entrainment function. *Journal of Fluid Mechanics*, 893, A12. doi:  
 873 <https://doi.org/10.1017/jfm.2020.225>

- 876 Cotte, L., Chavagnac, V., Pelleter, E., Laës-Huon, A., Cathalot, C., Dulaquais, G.,  
 877 ... Waeles, M. (2020). Metal partitioning after in situ filtration at deep-sea  
 878 vents of the lucky strike hydrothermal field (emso-azores, mid-atlantic ridge, 37  
 879 n). *Deep Sea Research Part I: Oceanographic Research Papers*, *157*, 103204.
- 880 Crone, T. J., McDuff, R. E., & Wilcock, W. S. (2008). Optical plume velocimetry: A  
 881 new flow measurement technique for use in seafloor hydrothermal systems. *Ex-  
 882 periments in fluids*, *45*, 899–915. doi: <https://doi.org/10.1007/s00348-008-0508-2>
- 884 Davies, J. H., & Davies, D. R. (2010). Earth's surface heat flux. *Solid earth*, *1*(1),  
 885 5–24. doi: <https://doi.org/10.5194/se-1-5-2010>
- 886 Devenish, B., Rooney, G., & Thomson, D. (2010). Large-eddy simulation of a buoy-  
 887 ant plume in uniform and stably stratified environments. *Journal of Fluid Me-  
 888 chanics*, *652*, 75–103. doi: <https://doi.org/10.1017/S0022112010000017>
- 889 Fiedler, H. (1988). Coherent structures in turbulent flows. *Progress in Aerospace  
 890 Sciences*, *25*(3), 231–269. doi: [https://doi.org/10.1016/0376-0421\(88\)90001-2](https://doi.org/10.1016/0376-0421(88)90001-2)
- 891 Fisher, C. R. (1998). Temperature and sulphide tolerance of hydrothermal vent  
 892 fauna. *Cah. Biol. Mar.*, *39*(3-4), 283–286.
- 893 Fontaine, F. J., Cannat, M., Escartin, J., & Crawford, W. C. (2014). Along-axis  
 894 hydrothermal flow at the axis of slow spreading mid-ocean ridges: Insights  
 895 from numerical models of the lucky strike vent field (mar). *Geochemistry,  
 896 Geophysics, Geosystems*, *15*(7), 2918–2931. doi: <https://doi.org/10.1002/2014GC005372>
- 898 Fox, D. G. (1970). Forced plume in a stratified fluid. *Journal of Geophysical Re-  
 899 search*, *75*(33), 6818–6835. doi: <https://doi.org/10.1029/JC075i033p06818>
- 900 Gao, X., Dong, C., Liang, J., Yang, J., Li, G., Wang, D., & McWilliams, J. C.  
 901 (2019). Convective instability-induced mixing and its parameteriza-  
 902 tion using large eddy simulation. *Ocean Modelling*, *137*, 40–51. doi:  
 903 <https://doi.org/10.1016/j.ocemod.2019.03.008>
- 904 Girard, F., Sarrazin, J., Arnaubec, A., Cannat, M., Sarradin, P.-M., Wheeler, B., &  
 905 Matabos, M. (2020). Currents and topography drive assemblage distribution  
 906 on an active hydrothermal edifice. *Progress in oceanography*, *187*, 102397. doi:  
 907 <https://doi.org/10.1016/j.pocean.2020.102397>
- 908 Hargreaves, D. M., Scase, M. M., & Evans, I. (2012). A simplified computational  
 909 analysis of turbulent plumes and jets. *Environmental fluid mechanics*, *12*, 555–  
 910 578. doi: <https://doi.org/10.1007/s10652-012-9250-7>
- 911 Hunt, G., & Kaye, N. (2001). Virtual origin correction for lazy turbulent plumes.  
 912 *Journal of Fluid Mechanics*, *435*, 377–396. doi: <https://doi.org/10.1017/S0022112001003871>
- 913 Hunt, G., & Kaye, N. (2005). Lazy plumes. *Journal of Fluid Mechanics*, *533*, 329–  
 914 338. doi: <https://doi.org/10.1017/S002211200500457X>
- 915 IOC, SCOR, IAPSO, et al. (2010). The international thermodynamic equation of  
 916 seawater, 2010: calculation and use of thermodynamic properties.
- 917 Jeong, J., & Hussain, F. (1995). On the identification of a vortex. *Journal of fluid  
 918 mechanics*, *285*, 69–94. doi: <https://doi.org/10.1017/S0022112095000462>
- 919 Jiang, H., & Breier, J. A. (2014). Physical controls on mixing and transport  
 920 within rising submarine hydrothermal plumes: A numerical simulation study.  
 921 *Deep Sea Research Part I: Oceanographic Research Papers*, *92*, 41–55. doi:  
 922 <https://doi.org/10.1016/j.dsr.2014.06.006>
- 923 Kaye, N. (2008). Turbulent plumes in stratified environments: A review of recent  
 924 work. *Atmosphere-ocean*, *46*(4), 433–441. doi: <https://doi.org/10.3137/ao.460404>
- 925 Kim, S. L., Mullineaux, L. S., & Helfrich, K. R. (1994). Larval dispersal via en-  
 926 trainment into hydrothermal vent plumes. *Journal of Geophysical Research:  
 927 Oceans*, *99*(C6), 12655–12665. doi: <https://doi.org/10.1029/94JC00644>
- 928 Kitamura, S., & Sumita, I. (2011). Experiments on a turbulent plume: Shape anal-

- 931                       yses. *Journal of Geophysical Research: Solid Earth*, 116(B3). doi: <https://doi.org/10.1029/2010JB007633>
- 932                       Koschinsky, A., Garbe-Schönberg, D., Sander, S., Schmidt, K., Gennerich, H.-H., &  
933                       Strauss, H. (2008). Hydrothermal venting at pressure-temperature conditions  
934                       above the critical point of seawater, 5 s on the mid-atlantic ridge. *Geology*,  
935                       36(8), 615–618. doi: <https://doi.org/10.1130/G24726A.1>
- 936                       Kotsovinos, N. E., & List, E. J. (1977). Plane turbulent buoyant jets. part 1. inte-  
937                       gral properties. *Journal of Fluid Mechanics*, 81(1), 25–44. doi: <https://doi.org/10.1017/S002211207700189X>
- 940                       Lavelle, J., Di Iorio, D., & Rona, P. (2013). A turbulent convection model with an  
941                       observational context for a deep-sea hydrothermal plume in a time-variable  
942                       cross flow. *Journal of Geophysical Research: Oceans*, 118(11), 6145–6160. doi:  
943                       <https://doi.org/10.1002/2013JC009165>
- 944                       Lee, R. W., Robert, K., Matabos, M., Bates, A. E., & Juniper, S. K. (2015).  
945                       Temporal and spatial variation in temperature experienced by macrofauna  
946                       at main endeavour hydrothermal vent field. *Deep Sea Research Part I: Oceanographic Research Papers*, 106, 154–166. doi: <https://doi.org/10.1016/j.dsr.2015.10.004>
- 947                       Lemaréchal, C., & Matabos, M. (2023). *Recording of a black smoker at the tour eif- fel vent field during momarsat2023*. SEANOE. doi: <https://doi.org/10.17882/103869>
- 948                       Lemaréchal, C., Roullet, G., & Gula, J. (2024a). *Coherent structures of a hydrothermal buoyant plume in the near-field obtained through les at ultra-high resolution*. Zenodo. doi: <https://doi.org/10.5281/zenodo.13829868>
- 949                       Lemaréchal, C., Roullet, G., & Gula, J. (2024b). *Parametric equation of state of sea- water for hydrothermal vent conditions*. Zenodo. doi: <https://doi.org/10.5281/zenodo.14332032>
- 950                       Marjanovic, G., Taub, G., & Balachandar, S. (2017). On the evolution of the plume  
951                       function and entrainment in the near-source region of lazy plumes. *Journal of Fluid Mechanics*, 830, 736–759. doi: <https://doi.org/10.1017/jfm.2017.622>
- 952                       Matulka, A., López, P., Redondo, J., & Tarquis, A. (2014). On the entrainment co-  
953                       efficient in a forced plume: quantitative effects of source parameters. *Nonlin-  
954                       ear processes in geophysics*, 21(1), 269–278. doi: <https://doi.org/10.5194/npg-21-269-2014>
- 955                       McDougall, T. J., Jackett, D. R., Wright, D. G., & Feistel, R. (2003). Accu-  
956                       rate and computationally efficient algorithms for potential temperature  
957                       and density of seawater. *Journal of Atmospheric and Oceanic Technology*,  
958                       20(5), 730–741. doi: [https://doi.org/10.1175/1520-0426\(2003\)20%3C730:AACEAF%3E2.0.CO;2](https://doi.org/10.1175/1520-0426(2003)20%3C730:AACEAF%3E2.0.CO;2)
- 959                       Mittelstaedt, E., Escartín, J., Gracias, N., Olive, J.-A., Barreyre, T., Davaille, A.,  
960                       ... Garcia, R. (2012). Quantifying diffuse and discrete venting at the tour  
961                       eiffel vent site, lucky strike hydrothermal field. *Geochemistry, Geophysics,  
962                       Geosystems*, 13(4). doi: <https://doi.org/10.1029/2011GC003991>
- 963                       Morton, B. (1959). Forced plumes. *Journal of Fluid mechanics*, 5(1), 151–163. doi:  
964                       <https://doi.org/10.1017/S002211205900012X>
- 965                       Morton, B., & Middleton, J. (1973). Scale diagrams for forced plumes. *Jour-  
966                       nal of Fluid Mechanics*, 58(1), 165–176. doi: <https://doi.org/10.1017/S002211207300220X>
- 967                       Morton, B., Taylor, G. I., & Turner, J. S. (1956). Turbulent gravitational convection  
968                       from maintained and instantaneous sources. *Proceedings of the Royal Society of  
969                       London. Series A. Mathematical and Physical Sciences*, 234(1196), 1–23. doi:  
970                       <https://doi.org/10.1098/rspa.1956.0011>
- 971                       Mullineaux, L. S., & France, S. C. (1995). Dispersal mechanisms of deep-sea hy-  
972                       drothermal vent fauna. *Geophysical Monograph Series*, 91, 408–424. doi:  
973                       <https://doi.org/10.1029/GM091p0408>

- 986 Pham, M., Plourde, F. d. r., & Kim, S. D. (2005). Three-dimensional characteriza-  
 987 tion of a pure thermal plume. *J. Heat Transfer*, *127*(6), 624–636. doi: <https://doi.org/10.1115/1.1863275>
- 988 Plourde, F., Pham, M. V., Kim, S. D., & Balachandar, S. (2008). Direct nu-  
 989 matical simulations of a rapidly expanding thermal plume: structure and  
 990 entrainment interaction. *Journal of Fluid Mechanics*, *604*, 99–123. doi:  
 991 <https://doi.org/10.1017/S0022112008001006>
- 992 Popinet, S. (2003). Gerris: a tree-based adaptive solver for the incompressible eu-  
 993 ler equations in complex geometries. *Journal of computational physics*, *190*(2),  
 994 572–600. doi: [https://doi.org/10.1016/S0021-9991\(03\)00298-5](https://doi.org/10.1016/S0021-9991(03)00298-5)
- 995 Popinet, S. (2009). An accurate adaptive solver for surface-tension-driven interfacial  
 996 flows. *Journal of Computational Physics*, *228*(16), 5838–5866. doi: <https://doi.org/10.1016/j.jcp.2009.04.042>
- 997 Popinet, S. (2013). *The basilisk code*. Retrieved from <http://basilisk.fr/>
- 998 Popinet, S. (2015). A quadtree-adaptive multigrid solver for the serre–green–naghdi  
 1000 equations. *Journal of Computational Physics*, *302*, 336–358. doi: <https://doi.org/10.1016/j.jcp.2015.09.009>
- 1001 Priestley, C., & Ball, F. (1955). Continuous convection from an isolated source of  
 1002 heat. *Quarterly Journal of the Royal Meteorological Society*, *81*(348), 144–157.  
 1003 doi: <https://doi.org/10.1002/qj.49708134803>
- 1004 Richardson, J., & Hunt, G. R. (2022). What is the entrainment coefficient of a pure  
 1005 turbulent line plume? *Journal of Fluid Mechanics*, *934*, A11. doi: <https://doi.org/10.1017/jfm.2021.1070>
- 1006 Safarov, J., Millero, F., Feistel, R., Heintz, A., & Hassel, E. (2009). Thermody-  
 1007 namic properties of standard seawater: extensions to high temperatures and  
 1008 pressures. *Ocean Science*, *5*(3), 235–246. doi: <https://doi.org/10.5194/os-5-235-2009>
- 1009 Sarrazin, J., Rodier, P., Tivey, M. K., Singh, H., Schultz, A., & Sarradin, P.-M.  
 1010 (2009). A dual sensor device to estimate fluid flow velocity at diffuse hy-  
 1011 drothermal vents. *Deep Sea Research Part I: Oceanographic Research Papers*,  
 1012 *56*(11), 2065–2074. doi: <https://doi.org/10.1016/j.dsr.2009.06.008>
- 1013 Sclater, J., Jaupart, C., & Galson, D. (1980). The heat flow through oceanic and  
 1014 continental crust and the heat loss of the earth. *Reviews of Geophysics*, *18*(1),  
 1015 269–311. doi: <https://doi.org/10.1029/RG018i001p00269>
- 1016 Shabbir, A., & George, W. K. (1994). Experiments on a round turbulent buoyant  
 1017 plume. *Journal of Fluid Mechanics*, *275*, 1–32. doi: <https://doi.org/10.1017/S0022112094002260>
- 1018 Sun, H., Feistel, R., Koch, M., & Markoe, A. (2008). New equations for density, en-  
 1019 tropy, heat capacity, and potential temperature of a saline thermal fluid. *Deep  
 1020 Sea Research Part I: Oceanographic Research Papers*, *55*(10), 1304–1310. doi:  
 1021 <https://doi.org/10.1016/j.dsr.2008.05.011>
- 1022 Tao, Y., Rosswog, S., & Brüggen, M. (2013). A simulation modeling approach to hy-  
 1023 drothermal plumes and its comparison to analytical models. *Ocean Modelling*,  
 1024 *61*, 68–80. doi: <https://doi.org/10.1016/j.ocemod.2012.10.001>
- 1025 Taub, G., Lee, H., Balachandar, S., & Sherif, S. (2015). An examination of the  
 1026 high-order statistics of developing jets, lazy and forced plumes at various axial  
 1027 distances from their source. *Journal of Turbulence*, *16*(10), 950–978. doi:  
 1028 <https://doi.org/10.1080/14685248.2015.1008006>
- 1029 Van Audenhaege, L., Matabos, M., Brind'Amour, A., Drugmand, J., Laës-Huon,  
 1030 A., Sarradin, P.-M., & Sarrazin, J. (2022). Long-term monitoring reveals  
 1031 unprecedented stability of a vent mussel assemblage on the mid-atlantic  
 1032 ridge. *Progress in Oceanography*, *204*, 102791. doi: <https://doi.org/10.1016/j.pocean.2022.102791>
- 1033 Van Dover, C. L. (2002). Community structure of mussel beds at deep-sea hy-  
 1034 drothermal vents. *Marine Ecology Progress Series*, *230*, 137–158. doi:  
 1035

- 1041 doi:10.3354/meps230137  
1042 Van Reeuwijk, M., & Craske, J. (2015). Energy-consistent entrainment relations for  
1043 jets and plumes. *Journal of Fluid Mechanics*, 782, 333–355. doi: <https://doi.org/10.1017/jfm.2015.534>  
1044  
1045 Van Reeuwijk, M., Salizzoni, P., Hunt, G. R., & Craske, J. (2016). Turbulent trans-  
1046 port and entrainment in jets and plumes: a dns study. *Physical Review Fluids*,  
1047 1(7), 074301. doi: <https://doi.org/10.1103/PhysRevFluids.1.074301>  
1048 Vic, C., Gula, J., Roullet, G., & Pradillon, F. (2018). Dispersion of deep-sea hy-  
1049 drothermal vent effluents and larvae by submesoscale and tidal currents. *Deep*  
1050 *Sea Research Part I: Oceanographic Research Papers*, 133, 1–18. doi: <https://doi.org/10.1016/j.dsr.2018.01.001>  
1051  
1052 Vreman, A. (2004). An eddy-viscosity subgrid-scale model for turbulent shear flow:  
1053 Algebraic theory and applications. *Physics of fluids*, 16(10), 3670–3681. doi:  
1054 <https://doi.org/10.1063/1.1785131>  
1055 Wang, H., & Law, A. W.-k. (2002). Second-order integral model for a round turbu-  
1056 lent buoyant jet. *Journal of Fluid Mechanics*, 459, 397–428. doi: <https://doi.org/10.1017/S0022112002008157>  
1057  
1058 Winters, K. B., Lombard, P. N., Riley, J. J., & D'Asaro, E. A. (1995). Available po-  
1059 tential energy and mixing in density-stratified fluids. *Journal of Fluid Mechan-  
1060 ics*, 289, 115–128. doi: <https://doi.org/10.1017/S002211209500125X>  
1061 Woods, A. W. (2010). Turbulent plumes in nature. *Annual Review of Fluid  
1062 Mechanics*, 42(1), 391–412. doi: <https://doi.org/10.1146/annurev-fluid-121108-145430>  
1063  
1064 Wykes, M. S. D., Hughes, G. O., & Dalziel, S. B. (2015). On the meaning of mix-  
1065 ing efficiency for buoyancy-driven mixing in stratified turbulent flows. *Journal  
1066 of Fluid Mechanics*, 781, 261–275. doi: <https://doi.org/10.1017/jfm.2015.462>  
1067 Xu, G., Jackson, D., Bemis, K., & Rona, P. (2013). Observations of the volume flux  
1068 of a seafloor hydrothermal plume using an acoustic imaging sonar. *Geochem-  
1069 istry, Geophysics, Geosystems*, 14(7), 2369–2382. doi: <https://doi.org/10.1002/ggge.20177>  
1070  
1071 Xu, G., McGillicuddy Jr, D., Mills, S., & Mullineaux, L. (2018). Dispersal of  
1072 hydrothermal vent larvae at east pacific rise 9–10 n segment. *Journal of Geo-  
1073 physical Research: Oceans*, 123(11), 7877–7895. doi: <https://doi.org/10.1029/2018JC014290>  
1074